

INNOVATIVE PROCESSES FOR
METAL OXIDE CERAMIC SYNTHESIS

By

AUDREY CELINE VECOVEN

Bachelor of Science

University of Lille I

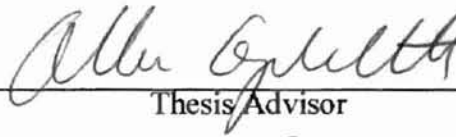
Villeneuve D'Ascq, France

1998

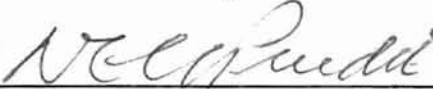
Submitted to the Faculty of the
Graduate College of the
Oklahoma State University
In partial fulfillment of
the requirements for
the Degree of
MASTERS OF SCIENCE
December, 2001

INNOVATIVE PROCESSES FOR
METAL OXIDE CERAMIC SYNTHESIS

Thesis Approved:



Thesis Advisor







Dean of the Graduate College

ACKNOWLEDGMENTS

Page

First and Foremost I would like to express my deepest thanks to my thesis advisor, Dr Allen W. Apblett, for his guidance, patience and support. I have been very fortunate to study under Dr Apblett these last two years. I will always carry with me his wisdom and enthusiasm.

I am especially grateful to Phoebe Doss for the Scanning and Transmission electron microscopy images.

I would like to thank my committee members, Dr Elizabeth Holt, Dr Allen W. Apblett, and Dr Neil Purdie.

I would like to acknowledge my fellow graduate, and friends for their support and encouragement.

I very much appreciate the help over the years of the department office staff, and the Air Force Office of Scientific Research for support of this research project.

TABLE OF CONTENTS

Chapter	Page
I. INTRODUCTION	1
A. Conventional Preparation Methods.....	3
B. Chemical Routes for Ceramics Synthesis.....	4
C. Modified Powder Process.....	6
D. Solution Growth Process.....	9
II. EXPERIMENTAL SECTION.....	12
A. Instrumentation and Chemicals.....	12
B. Nickel Ferrite Precursors.....	13
C. Zinc Ferrite Precursors.....	18
D. Solution Growth Method for Ni(OH) ₂ synthesis.....	20
III. RESULTS AND DISCUSSION.....	23
A. Modified Powder Process for Ferrites Synthesis.....	23
1. Introduction.....	23
2. Reaction Yield Analysis.....	26
3. Reaction Completion Temperatures.....	28
4. X-ray Study of Nickel Ferrite Formation.....	32
5. Morphology Study of Metal Ferrite.....	36
6. Ferrite Crystallite Size Study.....	44

Chapter	Page
7. Conclusion.....	51
B. Solution growth method	53
LIST OF TABLES	
1. Introduction.....	53
2. Determination of Solubility of Ni(OH) ₂ in Concentrated Aqueous Ammonia.....	Page 60
3. Ni(OH) ₂ Thin Film From Solution Growth Method.....	63
4. Aluminum Doped Ni(OH) ₂	67
5. Solution Growth Method For Nickel Ferrite Synthesis.....	73
6. Conclusion.....	76
IV. REFERENCES.....	77

LIST OF TABLES

Table	Page
1. Nickel Ferrite Precursors.....	17
2. Zinc Ferrite Precursors.....	19
3. Metal Oxide Yield at 450°C.....	28
4. Iron Oxide Powders Surface Area Measurements.....	32
5. Crystallite Size and Surface Area of ZnFe ₂ O ₄ Precursors at 450°C.....	45
6. ZnFe ₂ O ₄ Surface Areas.....	46
7. Nickel Hexa-ammine Concentration in Concentrated Aqueous Ammonia.....	60
8. Surface Areas of β and α nickel Hydroxides from Solution Growth Method.....	68
9. Al(OH) ₄ ⁻ Concentration in Concentrated Aqueous Ammonia (mol/L).....	68
10. Surface Area of Ni(OH) ₂ -γ-Fe ₂ O ₄ and NiFe ₂ O ₄ from Solution Growth.....	74

Figure	Page
1. Modified Powder Processing: Comparison of Conventional Powder Processing and Continuous Phase of Bimetallic Oxide Using Liquid Metallorganic Precursors.....	48

LIST OF FIGURES

Figure	Page
1. Modified Powder Processing: Comparison of Conventional Powder Processing and Continuous Phase of Bimetallic Oxide Using Liquid Metallorganic Precursors.....	7
2. Mechanism of Ferrite Formation by Nickel Oxide Coated Ferric Oxide Powders.....	8
3. Nickel and Zinc Ferrite Yields.....	27
4. Nickel Ferrite Processing Temperatures.....	30
5. Zinc Ferrite Processing Temperatures.....	31
6. XRD Powder Patterns of Ni(acac) ₂ -γ-Fe ₂ O ₃ Precursor at 300°C(a), 600°C(b), and 1000°C(c).....	33
7. XRD Powder Patterns of NiFe ₂ O ₄ (a), α-Fe ₂ O ₃ (b), γ-Fe ₂ O ₃ (c), NiO (d).....	34
8. TGA of Ni(acac) ₂ -γ-Fe ₂ O ₃ Precursor.....	35
9. SEM Images of Ni(acetate) ₂ -γ-Fe ₂ O ₃ Precursor at 450°C and 850°C.....	38
10. SEM of γ-Fe ₂ O ₃	39
11. SEM Images of Ni(acac) ₂ -γ-Fe ₂ O ₃ Precursor at 130°C, 450°C, and 1000°C.....	41
12. SEM Image of Zn(gluconate) ₂ -γ-Fe ₂ O ₃ Precursor at 850°C.....	42
13. XRD of α-Fe ₂ O ₃ (a), ZnO (b), ZnFe ₂ O ₄ (c), Zn(gluconate) ₂ -γ-Fe ₂ O ₃ Precursor Pryrolyzed at 600 and 850 °C	43
14. ZnFe ₂ O ₄ Crystalline Size Measurements.....	44

Figure	Page
15. Crystallite Size Distributions of Zn(acetate) ₂ , Zn(gluconate) ₂ , and Zn(acac) ₂ Pyrolyzed at 450°C.....	48
16. Crystallite Size Distributions of ZnFe ₂ O ₄ from γ -Fe ₂ O ₃ Precursors.....	49
17. Crystallite Size Distributions from Zn(gluconate) ₂ Precursors.....	50
18. Bode Diagram.....	54
19. Ni(OH) ₂ Deposition Rate Study.....	63
20. SEM Image Nickel Hydroxide from Solution Growth Method.....	64
21. XRD Patterns of β -Ni(OH) ₂ from Solution Growth Method and Precipitation out of Ni(NO ₃) ₂ solution.....	65
22. Infrared Spectrum of β -Ni(OH) ₂	66
23. TGA of β -Ni(OH) ₂	67
24. XRD of α -Ni _(1-x) Al _x (OH) _(2+x)	69
25. Infrared Spectrum of α -Ni _(1-x) Al _x (OH) _(2+x)	70
26. XRD of Solids from NaAl(OH) ₄ -Ni(OH) ₂ -conc. NH ₄ OH Solutions.....	72
27. TEM of α -Ni(OH) ₂ -NaAl(OH) ₄ Precipitate.....	72
28. SEM image of as-prepared Ni(OH) ₂ - α -Fe ₂ O ₃	75
29. SEM image of NiFe ₂ O ₄ from Pyrolysis of Ni(OH) ₂ - γ -Fe ₂ O ₃ at 900°C.....	75

INTRODUCTION

The advent of modern chemistry and materials science has expanded the employment of ceramics well beyond that of structural materials through the creation of advanced ceramics. Their uses span an extremely broad range of applications that take advantage of their highly varied electrical, magnetic and chemical properties. Traditional ceramics are those derived from naturally occurring raw materials, and include structural clayware such as bricks, pipes, cements, glasses and refractories. Advanced ceramics are produced by synthetic chemical routes or from naturally occurring materials that have been highly refined. Their uses depend on mechanical behavior, electrical, magnetic and chemical properties.

Ceramics are defined as “the group of non-metallic, inorganic solid materials produced by thermal processes”¹. As opposed to metals and plastics, ceramics are hard, non-combustible and usually non-oxidizable. They can be used in severe conditions, such as high-temperature, and corrosive environments. In addition, many ceramics, described as advanced or engineering ceramics, exhibit superior electronic, magnetic, optical or mechanical properties when prepared using the appropriate technique. Due to these unique characteristics, they have been increasingly sought for in industrial applications such as energy development, advanced telecommunications, and aeronautics.

Examples of applications of advanced ceramics include:

- Structural ceramics

(M) **Bioceramic** (9). The spinel ferrites, which are by far the most important in this class

(10) **Ceramic coatings** (10). For the most part, the new powdering method

- Mechanical seals
- High temperature oxide superconductors

of oxide ferrites (10) (11) (12) (13) (14) (15) (16) (17) (18) (19) (20) (21) (22) (23) (24) (25) (26) (27) (28) (29) (30) (31) (32) (33) (34) (35) (36) (37) (38) (39) (40) (41) (42) (43) (44) (45) (46) (47) (48) (49) (50) (51) (52) (53) (54) (55) (56) (57) (58) (59) (60) (61) (62) (63) (64) (65) (66) (67) (68) (69) (70) (71) (72) (73) (74) (75) (76) (77) (78) (79) (80) (81) (82) (83) (84) (85) (86) (87) (88) (89) (90) (91) (92) (93) (94) (95) (96) (97) (98) (99) (100)

Regardless of the application, the materials must be highly stoichiometric, homogeneous and of high purity, as each of these parameters is known to dramatically affect the chemical and physical properties.

Ceramic materials can be classified according to their elemental composition as metal nitrides, metal carbides, and metal oxide ceramics. The last category constitutes the most important class of ceramic materials.

There are two main avenues of research in the ceramic field. The first one deals with the development of new ceramic materials, and the second seeks one to improve the characteristics and/or production cost of already known materials by designing new preparation techniques. Our research is based on the second approach and our main objectives include the application of a new modified powder process with lower preparative temperatures to the preparation of ferrites, a technological-essential class of oxide ceramics. Ferrites are an important category of magnetic materials that have been used in inductors, transformers (NiFe_2O_4 and ZnFe_2O_4), and in microwave devices such as isolators and circulators (Yttrium-based garnets, MgFe_2O_4 and MnFe_2O_4). They are composed of iron oxide as the principle component, combined with a divalent metal oxide to yield spinel ferrites: $\text{M(II)Fe(III)}_2\text{O}_4$, or a with a trivalent metal oxide,

($M(III)_3Fe(III)_5O_{12}$). The spinel ferrites, which are by far the most important in this class of materials, were selected for the investigation of the new processing method.

A. Conventional Preparation Methods:

The conventional route for industrial production of metal oxide ceramic materials is through powder processing. This technique is based on high temperature processing of inexpensive raw materials. The conventional methods consist of mixing stoichiometric amounts of the corresponding oxide powders usually the metal oxides or carbonates (e.g. NiO and Fe_2O_3 for $NiFe_2O_4$ synthesis), after which the mixtures are ground. The powders are then calcined, sometimes after compaction; sintering can be repeated several times with intermediate grinding stages to optimize surface contact between particles. The phase boundary reaction occurs at the points of contact between the two components and later by counter diffusion of the metal cations through the product phase. The relative simplicity of this process and the use of cost effective components such as oxides and carbonates constitute the two major advantages of the powder processing method, also known as the “ceramic method”. However, the ceramic method suffers from several disadvantages such as:

- High temperature treatments, which can result in loss of volatile oxides. In the preparation of coatings from powders, high temperatures can also lead to irreversible deterioration of the substrate.

- With the progress of the reaction, the diffusion paths of the constituents through the product phase become longer and the reaction rate slower. The intermittent grinding

stages between heating cycles help, to some extent, optimize the surface contact between unreacted metal oxide particles.

- Limited compositional control: Due to lack of monitoring ability, the ideal experimental conditions that will lead the reaction to completion are determined by trial error. Therefore, the desired product is often mixed with small quantities of impurities such as reactants or intermediate phases.

- Incomplete chemical homogenization.

B. Chemical Routes for Ceramics Synthesis:

Various “pre-ceramic” routes have been developed to overcome those limitations and yield higher quality products with the desired shapes, forms, and purities for targeted applications. Most have the objective of decreasing the diffusion path lengths of metal ions by bringing down the particle size to a few hundred angstroms, and thus effect a more intimate mixing of the reactants. The main chemical routes applied to oxide ceramics synthesis according to a recent review² are:

- Metal Organic Chemical Vapor Deposition (MOCVD) techniques are based on the formation of ceramic materials from thermal decomposition of metal organic gases on a substrate. These methods are usually applied for deposition of thin films and allow large area deposition capability, excellent composition control, film uniformity, and the production of narrow size distribution nanophase particles. The main class of precursor applied to MOCVD includes metal alkoxides, metal alkyls, and metal β -diketonates. For example, Nickel and Zinc ferrite thin films were successfully grown by decomposition of the metal salts of tetramethyl heptanedionate and the metal salts of acetylacetonate³.

Unfortunately, MOCVD methods require high cost reactors and are also limited by the availability of volatile metal precursors possessing a large temperature window between evaporation and decomposition.⁴

- Spray drying and freeze-drying techniques are currently used industrially. The freeze-drying method converts a liquid phase to a solid phase by rapid cooling of the atomized solution. The desired product, a very fine powder, is obtained through sublimation of the solvent from the solid phase, followed by thermal decomposition. For example, the superconductor $\text{YBa}_2\text{CuO}_{(7-8)}$ was prepared by freeze-drying a solution of the corresponding metal nitrates and yielded a fine powder (particle size less than $5\ \mu\text{m}$) with greater compositional homogeneity than the conventional powder mixing process⁵.

- Hydrothermal oxidation and hydrolysis of metal organics. Examples of ferrite preparations by hydrolysis of metal acetylacetonates, pentadionates and alkoxides in aqueous ammonia or aminoalcohols have also been reported⁶⁻¹⁰.

- Solution routes usually involve co-precipitation of the ceramic precursor from homogenous solution followed by pyrolysis. Their numerous advantages over conventional methods include improved stoichiometry control of the metals, lower processing temperatures, and higher homogeneity. However they suffer from high cost of precursors, shrinkage during thermal processing, the presence of carbon in the final ceramics as a result of incomplete decomposition and, hence, the necessity for longer processing time to avoid carbon incorporation¹¹. Fe(II) oxalate is known to form solid solutions with a number of oxalates of other divalent metals such as Zn^{2+} , Co^{2+} , Ni^{2+} , Mg^{2+} and Mn^{2+} . Thermal decomposition of the oxalate solid solution precursors in the 800 to 1000°C range temperature yields fine ferrite particles¹¹. However, the iron(III) to

divalent metal ratio in the materials obtained deviates from ideality due to the different solubilities of the Fe^{2+} and M^{2+} oxalates and their tendency to form supersaturated solutions, unless the reaction conditions are carefully controlled¹². An excellent example of a crystalline precursor for stoichiometric ferrites is the mixed acetate, $\text{M}_3\text{Fe}_6(\text{CO}_2\text{-CH}_3)_{17}\text{O}_3(\text{OH})\cdot 12\text{pyridine}$ ($\text{M} = \text{Ni, Co, Mn}$) reported by Wickham et al.¹³. When heated to 800 to 1100°C this precursor yielded ferrites with a Fe(III):M(II) ratio that deviated by less than 0.01 from the ideal value of 2. While the mixed acetates were easily recrystallized, this process had the drawback of requiring pyridine. Another successful, inexpensive and more environmentally friendly precursor for nickel ferrite was prepared using sodium iron Ethylene Diamine TetraAceto and NiCl_2 ¹⁴. The resulting crystalline compound, $[\text{Ni}(\text{H}_2\text{O})_6][\text{FeCl}(\text{EDTA})\text{H}]_2\cdot x\text{H}_2\text{O}$ was pyrolyzed to 900°C leaving a crystalline residue consisting of stoichiometric nickel ferrite. Liquid metal carboxylates previously investigated in MOCVD methods have also been applied to nickel ferrite synthesis¹⁵.

C. Hybrid Route for Ferrite Synthesis: The Modified Powder Processing Method:

Combining the numerous advantages of each method developed a hybrid method, alternative to the cost-effective conventional technique and the expensive precursor methods of preparation of ceramics. This hybrid method consists of associating the economical aspect of the conventional powder process by using an inexpensive raw material as one reactant (such as Fe_2O_3 or Al_2O_3), and the strengths of chemical methods by coating the finely ground raw material particles with a second metal oxide phase. This approach is illustrated in Figure 1 (B) in comparison to conventional powder processing

(A). It provides a precursor mixture that has homogeneity intermediate between that of pure chemical routes and conventional powder processing, and since the ions have less distance to travel, the solid-state reactions are complete at lower temperatures and in less time. It was found that the precursor powder prepared by this method converted to an unusual foamed nanocrystalline ferrite at 800°C.

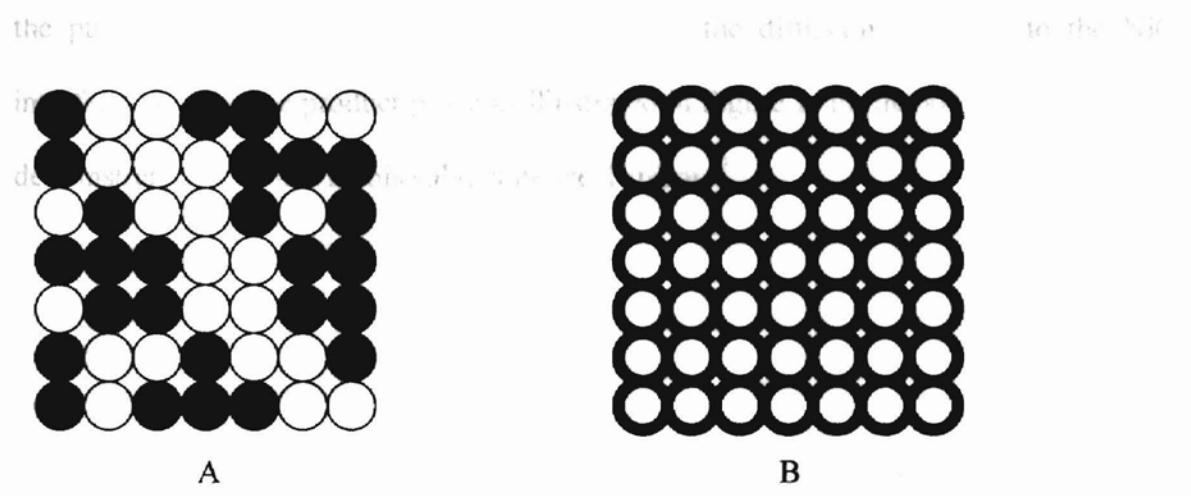


Figure 1. Modified powder processing: Comparison of (A) conventional powder processing and (B) continuous phase of a bimetallic oxide using liquid metallorganic precursors ¹⁶.

- The first application of the modified powder processing method involved the use of a finely ground ferric oxide and a liquid nickel carboxylate for the synthesis of nickel ferrite. The liquid metal carboxylate Ni(2-[2-(2-Methoxy)-Ethoxy]EthoxyAcetate)0.5H₂O (Ni(MEEA)₂.0.5H₂O) was employed to uniformly coat the hematite powder with a continuous film of NiO ¹⁶. Pyrolysis of the precursor to 500°C produced a powder with microscopic features similar to those of the starting iron oxide, suggesting a very homogeneous coating of Fe₂O₃ particles with NiO. This was attributed to a possible in-

situ CVD reaction during which $\text{Ni}(\text{MEEA})_2$ is partially volatilized at its decomposition point and uniformly deposited onto the Fe_2O_3 particles where it undergoes thermal decomposition to form NiO . Upon heating to 800°C the material was completely converted to small porous particles of trevorite, NiFe_2O_4 (crystallite size less than 18 nm). The striking difference of morphologies between the initial chunk-like particles and the puffed trevorite particles is accounted for by the diffusion of Fe_2O_3 to the NiO interface, through the product phase as illustrated in Figure 2. Formation of ZnFe_2O_4 was demonstrated to occur via this solid-state mechanism ¹⁷.

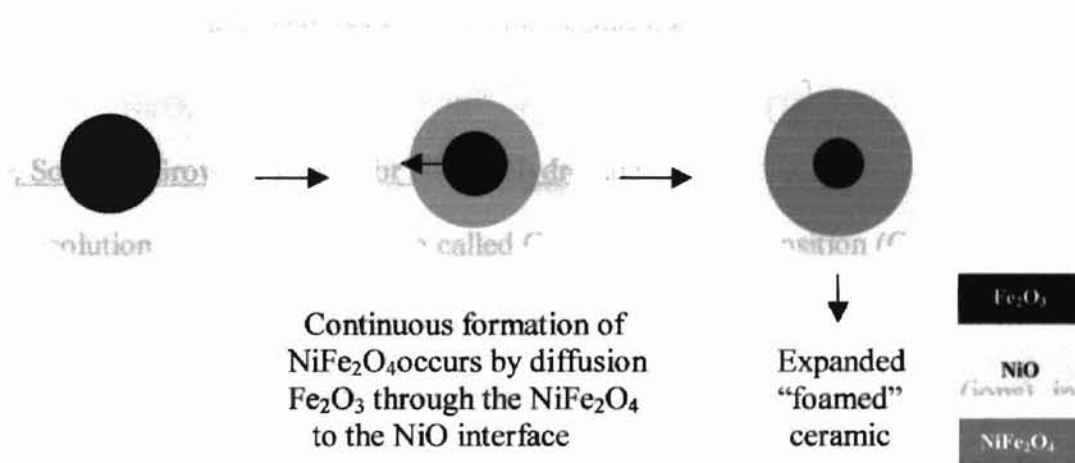


Figure 2. Mechanism of ferrite formation by nickel oxide coated ferric oxide powders ¹⁸.

Other MEEA salts were also successfully applied to ceramics preparation using the modified powder processing described above. For example MgAl_2O_4 was obtained using $\text{Mg}(\text{MEEA})_2 \cdot 2\text{H}_2\text{O}$ and aluminum oxide. However, the morphology of the final product did not exhibit the same features as NiFe_2O_4 described above ¹⁸. Despite the proven

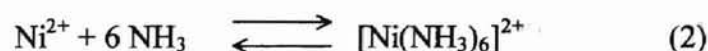
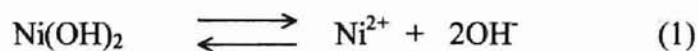
usefulness of the liquid MEEA for the preparation of spinels, its high cost renders any potential industrial application unlikely.

This research focuses on the application of the modified powder processing method for low temperature preparation of ferrites by utilizing more economical precursors. In this study, a variety of metal carboxylates were applied to the modified powder processing method, and the nature of the metal organic compound correlated with the morphology (microscopy, surface area, crystallite size) of the desired final product and the processing temperature necessary for completion of the solid state reaction. In addition to the influence of the metal carboxylate characteristics on the final product, the nature of the starting iron oxide source was also investigated. The six coordination compounds investigated were Nickel and Zinc acetates, gluconates, and acetylacetonates.

D. Solution Growth Method for Nickel Hydroxide:

The solution growth method, also called Chemical Bath Deposition (CBD) of films is similar to the Chemical Vapor Deposition (CVD) in the gas phase. The film growth takes place “via reaction near room temperature between dissolved precursors (ions) in a metastable environment”¹⁹. This technique has been thoroughly investigated for the deposition of sulfide films such as CdS²⁰, $Pb_{(1-x)}Hg_xS$ ²¹ or ZnS²², which have important applications as optoelectronic materials. For example, uniform CdS films were grown from an aqueous alkaline solution containing thiourea, which provided the sulfur ions, and cadmium-ammonia complex ions. Under basic conditions $SC(NH_2)_2$ is slowly hydrolyzed, releasing sulfide ions that combine with metal ions to form films on substitutes immerse in the chemical bath²². A slightly different approach was developed

for the growth of ammonium dihydrogen phosphate crystals. The growth solution consisted of a saturated aqueous solution of ADP prepared at 45°C. Crystal growth was initiated by a highly controlled temperature decrease to 30°C (0.1 to 0.3°C/day)²³. The solution growth method for preparation of films of nickel hydroxide was also investigated as a very inexpensive method of coating iron oxide particles with NiO. The solution growth process could also be used for the growth of Ni(OH)₂ films for electrode materials. The method involves dissolution of Ni(OH)₂ in concentrated aqueous ammonia as nickel hexa-ammine complex (see equations 1 and 2). As ammonia evaporates, the equilibria of equations 1 and 2 are displaced to the left, resulting in the slow precipitation of nickel hydroxide in the form of a thin film.



Ni(OH)₂ occurs in two crystallographic forms, one of which is isomorphous with Mg(OH)₂ and is called β nickel hydroxide. The second form, alpha Ni(OH)₂, is actually a series of compounds containing a variable excess of water molecules and foreign ions intercalated between NiO₂ slabs²⁴. The conventional α-Ni(OH)₂ designation for such compounds includes a large set of disordered Ni(II) hydroxides which tend to convert to the beta phase in alkaline media. α-Ni(OH)₂ has been shown to be a better electrode material, and therefore is of great interest to battery manufacturers who devoted numerous studies to the development of new processes for stabilization of α-Ni(OH)₂. A common technique consists of the stabilization of the alpha form through partial

substitution of nickel(II) with aluminum(III) resulting in the formation of a Double-Layered-Hydroxide. The doping of Ni(OH)_2 with Al(III) using the solution growth process was attempted by saturating the solution growth bath with aluminum hydroxide, as a first approach, and by addition of a sodium aluminate solution to the Ni(OH)_2 -saturated concentrated ammonia solution.

The nickel hydroxide solution growth process was applied in this investigation to synthesis of trevorite (NiFe_2O_4) as a means of coating fine iron oxide particles with Ni(OH)_2 which resulted in a highly homogeneous and inexpensive ceramic-precursor .

As with the field of ceramics in general, improvements in the properties of ferrites have been made through close control of preparation conditions and innovations in processing. The research reported herein is based on the development and application of a new economic procedure for ferrite synthesis with reduced processing temperatures through uniform coating of iron oxide particles with divalent metal oxides. The new preparative methods allow for improved homogeneity and phase purity as compared to conventional powder processing and also provide the ability to control the microstructure of the resulting ceramic materials.

EXPERIMENTAL SECTION

A. Instrumentation and Chemicals

All chemicals were of reagent purity and were used without further purification. Aluminum powder (Valimet), Nickel hydroxide $\text{Ni}(\text{OH})_2$ (Strem), Nickel acetate $\text{Ni}(\text{CH}_3\text{CO}_2)_2 \cdot 4\text{H}_2\text{O}$ (Aldrich), Nickel acetylacetonate $\text{Ni}(\text{C}_5\text{H}_5\text{O}_2)_2 \cdot 11.2\% \text{H}_2\text{O}$ (Strem), Nickel oxide NiO (Strem), Aqueous ammonium hydroxide NH_4OH ACS reagent (Scientific Products), Zinc Acetate $\text{Zn}(\text{CO}_2\text{CH}_3)_2 \cdot 2\text{H}_2\text{O}$ (Aldrich), zinc acetylacetonate $\text{Zn}(\text{C}_5\text{H}_5\text{O}_2)_2 \cdot 7.5\% \text{H}_2\text{O}$ (Strem), zinc gluconate $\text{Zn}(\text{C}_6\text{H}_{11}\text{O}_7)_2$ (Alpha Aesar), Alpha iron oxy-hydroxide αFeOOH (Strem), gamma iron oxide $\gamma \text{Fe}_2\text{O}_3$ (Nanophase), Ferric oxide (coarse) Fe_2O_3 (Fisher Scientific), α Iron oxide (hematite) high purity Fe_2O_3 (Puratronic, Alpha Aesar), Ferrous gluconate $\text{Fe}(\text{II})(\text{C}_6\text{H}_{11}\text{O}_7)_2 \cdot 2\text{H}_2\text{O}$ (Alpha Aesar), Ferric acetylacetonate $\text{Fe}(\text{III})(\text{C}_5\text{H}_5\text{O}_2)_3$ (Strem), Ferrous chloride $\text{FeCl}_2 \cdot 4\text{H}_2\text{O}$ (Aldrich), ferric chloride $\text{FeCl}_3 \cdot 6\text{H}_2\text{O}$ (Matheson, Coleman & Bell), sodium hydroxide (Spectrum), Sodium nitrite NaNO_2 (Fisher Scientific), hexamethylenetetramine $\text{N}_4(\text{CH}_2)_6$ (Matheson, Coleman & Bell), Ethyl alcohol $\text{CH}_3\text{CH}_2\text{OH}$ USP grade (Pharmco Products), N,N dimethylformamide (E.M. Science), D-gluconic acid 45-50% solution $\text{C}_6\text{H}_{12}\text{O}_7$ (Aldrich). Water was purified by reverse osmosis and then deionized before use. Thermogravimetric studies were performed on a Seiko EXSTAR 6000 TG/DTA 6200 instrument under a

100ml/min flow of nitrogen. Infrared spectra were collected by diffuse reflectance of ground powder diluted in KBr on a Nicolet Magna-IR 750 FTIR Spectrometer. Bulk pyrolyses at various temperatures were performed in ambient air in a temperature programmable muffle furnace using a temperature ramp of 1°C/min and a hold time of 14 hours. X-ray powder diffraction patterns were obtained on a Bruker AXS D8 Advance diffractometer using copper $K\alpha$ (1.5418 Å) radiation. Surface area measurements were performed on a Quantachrome Nova 1200 instrument by nitrogen adsorption and the BET six-point methods. Samples were prepared prior to surface analysis by degassing under vacuum at 100°C. Scanning electron micrographs were taken on a JEOL JXM 6400 Scanning Electron Microscope.

B. Precursor Synthesis for $NiFe_2O_4$

Nickel gluconate hydrate preparation:

1.86 grams (0.020 moles) of $Ni(OH)_2$ and 17.44 grams of a 45-50% solution (0.040 moles) of D-gluconic acid were added to 250 ml of distilled water. The solution was heated under reflux and with constant stirring for two days. The resulting green solution was concentrated by evaporating 2/3 of the solvent under reduced pressure in a water bath at a temperature range of 50-60°C. Nickel gluconate was isolated by precipitation from the dark green solution after addition of 700 ml of methanol. The resulting pale green solid was collected by filtration using a medium porosity fritted glass filter, then washed twice with 200 ml of methanol, and dried under vacuum overnight. The reaction yielded 8.11 g (yield: 83.69%). Nickel gluconate hydrate $Ni(C_6H_{11}O_7)_2 \cdot 2H_2O$.

(484.69g/mol). IR (cm^{-1})(KBr) 3498(s,br), 2886(s), 2823(m), 1642(s), 1553(m), 1479(m), 1295(m), 1138(m), 1103(m), 885(m), 749(s)

Lepidocrocite (γ FeOOH) preparation ²⁵:

59.6 grams (0.302 moles) of ferrous chloride tetrahydrate was dissolved in 1.5 liters of deionized water, followed by filtration of residual $\text{Fe}(\text{OH})_3$. The filtrate was added to a solution of 83.9 grams (0.600 moles) of hexamethylenetetraamine in 300 ml of distilled water. A blue green precipitate ($\text{Fe}(\text{OH})_2$) formed. Then a solution of 21.0 grams (0.304 moles) of sodium nitrite was added with constant stirring. The mixture was heated to about 60°C and allowed to stand for three hours with occasional agitation. The oxidation that produces γ -FeOOH proceeded with evolution of considerable quantities of nitrous oxide gas. The supernatant liquid was drained off and the precipitate was washed thoroughly with warm water and dried at 60°C in an air oven overnight. The reaction yielded 26.2 grams (97.7%). IR (cm^{-1})(KBr) 3196(s,br), 1891 (m), 1635(m), 1506(m), 1346(w), 1166(m), 1024(s), 880(w), 747(m).

Hematite (α Fe_2O_3) nanoparticle synthesis ²⁶:

1.08 grams (4.00 mmoles) of $\text{FeCl}_3 \cdot 6\text{H}_2\text{O}$ were added to 200 ml of water containing 0.0125 gram (0.0901 mmole) of $\text{NaH}_2\text{PO}_4 \cdot \text{H}_2\text{O}$. The solution was heated in a tightly capped Pyrex flask in a preheated oven at 100°C for 2 days and 17 hrs. The resulting orange suspension was centrifuged until the solution turned clear and a brown solid accumulated at the bottom of the plastic tube. The desired product, Fe_2O_3 , was collected

by filtration using a 20 μ m nylon membrane and washed with 200 ml of distilled water. The fine powder was dried under vacuum in air overnight.

General procedure for precursor preparation:

The experiments listed in Table 1 consisted of the pyrolysis of 5 mmoles of Ni(L)₂ with 5 mmoles of an iron oxide powder of specific form (α , γ), or 10 mmoles of Fe(L)₃, or Fe(L)₂ with 5 mmoles of NiO powder, L being an acetate, gluconate, or acetylacetonate ligand. Due to the small amount available of nanoparticulate Fe₂O₃, experiment #5 was prepared with only 2.2 mmoles of Ni(acetate)₂ and 2.2 mmoles of Fe₂O₃. A predetermined volume of the appropriate solvent was added to the metal-organic reactant and gently heated (about 50°C) to obtain a clear homogeneous solution. The metal oxide powder was rapidly added to the warm solution and slowly stirred as the precursor cooled down and thickened to a paste. The first combustion at 450°C was performed in a muffle furnace using a 1°C/min heating rate in a Pyrex beaker. The brown solid collected was then weighed and ground. A fraction was conserved in a vial for X-ray and microscopy studies while the rest was pyrolyzed to 800°C. Reaction completion temperature was determined by collecting the X-ray diffraction pattern of the sintered sample, starting at 800°C, and working by increments of 50°C until disappearance of the starting metal oxide peaks.

Metal gluconates and acetates are common water-soluble organometallic compounds. Water 2.5 ml was sufficient to dissolve the metal precursor as described above. Exp. #5 only required 1ml. On the other hand the solubility of metal acetylacetonates in water was not sufficiently high to reach complete dissolution of the metal precursor, even under

heating. N,N-Dimethylformamide (DMF) was instead preferred and only necessitated 2 mL to appropriately dissolve the precursor. In order to estimate the importance of the solvent on the solid-state reaction completion, Experiment #4 was carried out without addition of water.

All pyrolyzed samples apparently possessed similar morphological aspects (compact powders) with the exception of experiments which included Nickel(II) and Fe(II) gluconate, whose thermal decompositions were accompanied by a “foaming” process, yielding powders with higher surface area.

Table 1. Nickel Ferrite Precursor Compositions

#	Nickel source	Weight	Iron source*	Weight	Solvent	NiFe ₂ O ₄ **
1	Nickel gluconate	2.43	α Fe ₂ O ₃ HP	0.799	H ₂ O	1.104
2	Nickel acetate	1.25	α Fe ₂ O ₃ HP	0.799	H ₂ O	1.16
3	Nickel acetate	1.25	α Fe ₂ O ₃	0.799	H ₂ O	1.15
4	Nickel acetate	1.24	α Fe ₂ O ₃ HP	0.799	H ₂ O	1.16
5	Nickel acetate	0.55	α Fe ₂ O ₃ NP*	0.351	H ₂ O	0.501
6	Nickel acetyl acetate	1.46	α Fe ₂ O ₃ HP	0.800	DMF	1.17
7	Nickel gluconate	2.42	γ Fe ₂ O ₃	0.799	H ₂ O	1.12
8	Nickel acetate	1.25	γ Fe ₂ O ₃	0.800	H ₂ O	1.13
9	Nickel acetyl acetate	1.44	γ Fe ₂ O ₃	0.798	DMF	1.12
10	Nickel gluconate	2.42	γ FeOOH	0.994	H ₂ O	1.16
11	Nickel acetate	1.24	γ FeOOH	0.993	H ₂ O	1.16
12	Nickel acetyl acetate	1.44	γ FeOOH	0.995	DMF	1.16
13	Nickel acetate	1.24	α FeOOH	0.858	H ₂ O	1.13
14	NiO	0.372	Iron (III) acetyl acetate	3.53	DMF	1.12
15	NiO	0.373	Iron (II) gluconate	4.82	H ₂ O	1.13

* NP: Nano particles HP: High purity

** yields are in mol%

Weights in grams

C. Synthesis of Precursors for ZnFe₂O₄:

General procedure for precursor preparation:

The preparation of precursors for zinc ferrite was identical to that for nickel ferrite. A predetermined volume of the appropriate solvent is added to 5 mmoles of the metal-organic reactant and gently heated (about 60°C) to obtain a homogeneous clear solution. The metal oxide powder is rapidly added to the warm solution and gently stirred as the precursor cools down and thickens to a paste. The consistency of the precursors after cooling was visibly different from that of the nickel ferrite precursors: The samples did not harden in a thick solid but instead retained a very homogeneous gel-like appearance. The products of pyrolysis at 450°C provided valuable information concerning the sample homogeneity and decomposition process. The precursors prepared with zinc acetate hydrate (see Exp # 2, 5, 8, 10) yielded a brownish-red powder covered with a very fine white particles of ZnO, suggesting a poor coating of the iron oxide particles.

The thermal decomposition of precursors containing metal gluconate produced powders, which exhibited similar features to those observed for nickel ferrite preparations: large volume and apparent high surface area (58.8 m²/g).

The precursor compositions and the various solvents used for sample preparations are showed in Table 2.

Table 2. Zinc Ferrite Precursor Compositions

#	Zinc source	Weight	Iron source*	Weight	Solvent	ZnFe ₂ O ₄ **
1	Zinc gluconate	2.55	α Fe ₂ O ₃ HP	0.798	H ₂ O	1.18
2	Zinc acetate	1.10	α Fe ₂ O ₃ HP	0.793	H ₂ O	1.09
3	Zinc acetyl acetate	1.42	α Fe ₂ O ₃ HP	0.799	DMF	1.127
4	Zinc gluconate	2.55	γ Fe ₂ O ₃	0.793	H ₂ O	1.18
5	Zinc acetate	1.10	γ Fe ₂ O ₃	0.799	H ₂ O	1.12
6	Zinc acetyl acetate	1.42	γ Fe ₂ O ₃	0.799	DMF	1.11
7	Zinc gluconate	2.55	γ FeOOH	0.993	H ₂ O	1.20
8	Zinc acetate	1.10	γ FeOOH	0.994	H ₂ O	1.19
9	Zinc acetyl acetate	1.42	γ FeOOH	0.995	DMF	1.18
10	Zinc acetate	1.10	α FeOOH	0.858	H ₂ O	1.16
11	ZnO	0.407	Iron acetyl acetate	3.53	DMF	1.19
12	ZnO	0.408	Iron gluconate	4.82	H ₂ O	1.19

* HP: High purity

** yields in mol%

Weight: grams

D. Solution Growth Process for Nickel hydroxide synthesis:

Beta Nickel Hydroxide Synthesis:

Concentrated ammonium hydroxide (40 ml) was saturated with nickel hydroxide by stirring with 2 grams of Ni(OH)_2 for 1 hour and thirty minutes in a 50 ml beaker at room temperature. Excess Ni(OH)_2 was collected by filtration using a 20 μm nylon membrane and stored under vacuum overnight. The blue solution was stored in the fume hood until complete evaporation of the solvent; as NH_3 is slowly evolved, Ni(OH)_2 was deposited as a thin film on the flask walls. The precipitate was collected, placed under vacuum overnight and weighed. IR (cm^{-1})(KBr) 3638 (s, sh), 1483 (m), 1355 (m), 833 (w), 582 (m)

Concentration of $[\text{Ni(NH}_3)_6]^{2+}$ in saturated ammonia solution:

The solubility product, P_s of nickel hydroxide in concentrated aqueous ammonia was determined using the weight of solid deposited by complete evaporation of a known amount of saturated solution.

Alpha Nickel Hydroxide Preparation by Substitution with Aluminum(III):

- Stabilization of $\alpha\text{-Ni(OH)}_2$ by addition of Al(OH)_3 to ammonium hydroxide solution: Prior to adding Nickel hydroxide, 40 ml of NH_3 solution was saturated with aluminum hydroxide. The time necessary for the solution to reach saturation was estimated at 45 min. Excess Al(OH)_3 was filtered using a pre-weighed nylon membrane and placed under vacuum overnight. The exact Al^{3+} content of the solution was

determined by subtracting the weight of $\text{Al}(\text{OH})_3$ introduced in the solution from that of the excess solid previously filtered. Weight: 0.0618 grams in 40 ml NH_4OH solution. $[\text{Al}^{3+}] = 0.022$ mol/L present in the amine complex form.

Excess $\text{Ni}(\text{OH})_2$ powder was then added and the nickel saturated solution was isolated as described above. The light green solid collected after evaporation of solvent was put under vacuum and weighed (0.565 grams).

IR(KBr)(cm⁻¹) 3517(s,br), 2985(m), 2831(m), 1497(m,sh), 1355(s,sh), 870(m,br), 450(w).

- Stabilization of $\alpha\text{-Ni}(\text{OH})_2$ by addition of a sodium aluminate solution to solution growth bath:

Sodium aluminate solution (0.33 M):

Aluminum powder (1.78 grams, 0.066 mole) was slowly added to 200 ml of freshly distilled water containing an excess (6.03 grams, 0.15 mole) of NaOH. The highly exothermic reaction proceeded with rapid evolution of hydrogen gas and was carried out in an icy water bath and under careful stirring.

The amount of sodium aluminate necessary for stabilization of the alpha structure was determined by addition of increasing volumes of the 0.33 M $\text{NaAl}(\text{OH})_4$ solution to 40 ml of $\text{Ni}(\text{OH})_2\text{-NH}_3$ solutions. The $\text{Ni}(\text{OH})_2$ phase precipitated was identified by X-Ray diffraction and infrared spectroscopy. $\text{NaAl}(\text{OH})_4$ solution (6 ml of the 0.33 M) was the volume required for addition to 40 ml of the growth solution, for the stabilization of alpha nickel hydroxide. IR (cm⁻¹)(KBr) 3457 (s,br), 1360 (s), 854 (br).

Solution Growth Process for Nickel Ferrite synthesis:

0.904 grams (5.66 mmoles) of $\gamma\text{-Fe}_2\text{O}_3$ were added to 42 ml of $\text{NH}_3\text{-Ni(OH)}_2$ solution in a 500 ml high density polyethylene bottle with a narrow neck. Proper stirring was provided by horizontal rotation of the opened bottle on a roller mill. As NH_3 slowly evaporated a brown precipitate formed. After a month and a half, all the solvent has evolved and the brown solid accumulated on the bottle wall was scraped off and weighed. Total yield: 1.48 grams. Weight expected for stoichiometric proportions: 1.43 grams. IR (cm^{-1})(KBr) 3637(s,s), 3436(m,br), 1601(m), 1384(m,s), 1073(w), 833(w), 696(m), 643(m), 446(w), 424(w). Thermal decomposition at 900°C of 0.492 grams of sample yielded 0.400 grams of dark brown nickel ferrite. Yield: 90.52 %

RESULTS AND DISCUSSION

A. Modified Powder Process for Ferrites Synthesis:

1. Introduction:

- Structure of ferrites

The term “ferrite” is used to describe a class of magnetic oxide compounds, which contain iron oxide as a principle component ²⁷ and includes both the garnet and spinel crystal structures. Among the different types of ferrites, the spinel ferrites, which are isostructural to $MgAl_2O_4$, are by far the most important in this class of materials. Their common formula is MFe_2O_4 , where M stands for divalent metals such as Nickel(II), Copper(II), Zinc(II) etc. Their structure is based on a cubic close packed arrangement of anions (O^{2-}) in which cations occupy the interstitial sites in an ordered manner. A single unit cell of the spinel structure is composed of four atoms of oxygen, eight tetrahedral sites and four octahedral sites. In the case of the *normal* spinel structure, the Fe^{3+} cations half of the octahedral sites occupy while the M^{2+} cations occupy one-eighth of the tetrahedral holes. However certain compounds adopting the spinel structure, known as *inverse* spinels, possess a different arrangement of cations where the M^{2+} cations occupy octahedral sites and the Fe^{3+} cations are equally distributed between octahedral and tetrahedral sites.

- Applications of ferrites:

Spinel ferrites combine a wide range of useful magnetic properties with relatively low electrical conductivity. Thus unlike magnetic alloys and metals, they display low eddy current loss in alternating current applications and they are particularly useful in the radio frequency range. The magnetic moment of the ferrite materials arises from the unpaired d-electrons of the metal transition ions of both iron and M. Within the solid structure these magnetic moments align themselves through interaction with the bridging oxygen anions (the superexchange interaction), whereby the moments of both Fe^{3+} and M^{2+} are aligned, but are anti parallel to each other. The resulting magnetic moment per formula unit is, therefore, a superposition of these two antiparallel magnetic moments. The spinel ferrites magnetic properties have led to numerous applications in recording heads, core materials for transformers, inductors, TV deflection units and recording tape²⁷. Philips first commercially introduced them under the trademark "Ferrocube"²⁸. Ferrite powders can also be used to fabricate microwave elements such as isolators, phase shifters, circulators and limiters.

In addition to electronic components, ferrites have also been used as catalysts for a variety of reactions such as selective N-monomethylation of aniline catalyzed by $\text{Zn}_{(1-x)}\text{Co}_x\text{Fe}_2\text{O}_4$ and $\text{Zn}_{(1-x)}\text{Ni}_x\text{Fe}_2\text{O}_4$ ^{29,30}, and non oxidative dehydrogenation of cyclohexanol over $\text{Cu-Fe}_3\text{O}_4$ ³¹. Their catalytic strength is attributed to the ease with which iron changes oxidation states between +II and +III. A valuable advantage, from a commercial standpoint, is their good stability under highly reducing reaction conditions:

while Fe_2O_3 catalysts lose their activity upon reduction to FeO and Fe metal, the spinel lattice is retained as reduction of Fe^{3+} to Fe^{2+} takes place, allowing reoxidation to the original state. Magnesium ferrite belongs to a class of catalysts that are very effective for oxidative dehydrogenation of hydrocarbons with 4 to 6 carbon atoms; Goodrich-Gulf Chemicals developed superior commercial catalysts, $\text{MgCrFe}_2\text{O}_4$ and $\text{ZnCrFe}_2\text{O}_4$, for oxidative dehydrogenation of butene to butadiene^{32,33}. A previous study on the dehydrogenation of isopropanol over MgFe_2O_4 demonstrated that decomposition of the alcohol takes place on the Fe^{3+} sites. Adsorption of the isopropanol molecules, the rate-limiting step, occurs by transfer of electrons from the adsorbate to Fe^{3+} , this process is facilitated by a low n-type conductivity activation energy³⁴. This is consistent with the fact that the catalytic activity was attenuated when the ratio of $(\text{Fe}^{3+})_{\text{octa}} / (\text{Fe}^{3+})_{\text{tetra}}$ decreased, $\text{Fe}^{3+}_{\text{octa}}$ being more readily available to isopropanol molecules than $\text{Fe}^{3+}_{\text{tetra}}$. Therefore the catalytic activity largely depends on the cation distribution and also correlates with the electrical and magnetic properties of the ferrite catalyst investigated.

This research is focused on the development of a new method for preparation of metal ferrites, with the main objectives being the synthesis of stoichiometric ferrites at low temperatures by combining a metal oxide powder and a metal organic compound. Other attributes for the new techniques included phase purity, simplicity of the procedure, and economic viability. This new “modified powder processing” method, which allows the use readily available chemicals, has the ability of yielding advanced ceramic materials at a much lower cost than common chemical techniques. It may also be less expensive than conditional powder processing once costs of fuel and rejected products are factored in.

The approach initially adopted for the sample preparation consisted of the dissolution of the metal-organic compound in 50 mL of water, followed by the addition of a stoichiometric amount of metal oxide powder. Removal of the solvent by rotary evaporation at 1.9 Torr in a 60°C water bath yielded a very inhomogeneous looking dark-green solid. It was concluded, that this method was inappropriate for oxide particle coating due to the low solubility of certain metal-organic compounds in water. The solvent removal step caused the acetylacetonate compound to precipitate on the surface of the flask and form large green aggregates. Consequently the more convenient and rapid “crucible” technique as it had been reported earlier¹⁵ was chosen.

2. Reaction Yields Analysis:

All experiments formed ferrites with yields below complete conversion of the reagents, as listed in Table 1 and 2, but since unreacted metal oxide peaks were seldom observable on X-ray powder patterns, the stoichiometry seems to have been conserved. However, when grouping the precursors according to the type of iron oxide utilized, nickel and zinc ferrite yields exhibit similar trends as shown in Figure 3. Yields were closest to total conversion for samples containing gamma iron oxyhydroxide (NiFe_2O_4 precursors 10, 11, 12, and ZnFe_2O_4 precursors 7, 8, 9). The commercially available iron oxide powders were used without further purification or drying, and, therefore, may have contained adsorbed molecules unaccounted for in the molecular weight. In the case of iron oxyhydroxide, which had to be prepared, a small amount of iron reagent was pyrolyzed to 450°C to determine the exact water content and molecular weight. Thus the yield of ferrites from $\gamma\text{-FeOOH}$ were closest to unity.

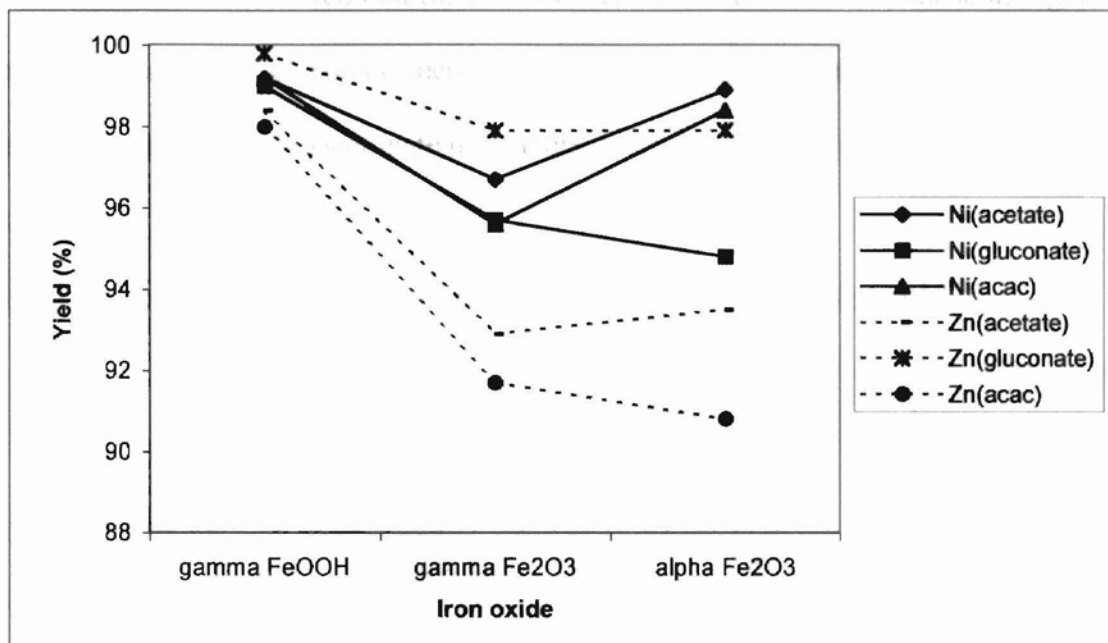


Figure 3. Nickel and Zinc Ferrite Yields (mol%)

In addition to molecules adsorbed on oxide powders, partial evaporation of the metal organic precursor during thermal decomposition can also account for low yields. Depending on the ligand and the metal atom, a small fraction of the compound is evolved and undergoes pyrolysis in the gas phase. The extent of this effect was evaluated for each precursor by heating a pre-weighed amount of the metal organic compound at 450°C. The resulting powder was considered to be pure metal oxide, since 450°C is well above the decomposition temperatures of most of the metalorganic compounds utilized. The metal oxide yields reported in Table 3 illustrates the degree of volatility of each organometallic reagent. Acetylacetonate metal salts are common reagents for Chemical Vapor Deposition and have high volatility, a subsequent fraction of $M(acac)_2$ evolved during

thermal treatment is deposited back onto the precursor surface, but a small amount is not recovered. It should be noted that the trends observed in Table 3 match those in Figure 3; precursors containing gluconate metal salts produced ferrites in markedly higher yields than did acetate and acetylacetonate precursors.

Table 3. Metal Oxide yield at 450°C from Pyrolysis of M(II)(L)₂ (mol %)

Ni(gluconate) ₂ - 2H ₂ O	98.1
Ni(acac) ₂ - H ₂ O	97.2
Ni(acetate) ₂ - 2H ₂ O	99.89
Zn(gluconate) ₂ - H ₂ O	100
Zn(acac) ₂ - H ₂ O	92.57
Zn(acetate) ₂ - H ₂ O	94.88

3. Reaction Completion Temperatures:

The plots of reaction completion temperatures of nickel ferrite and zinc ferrite versus iron oxide form are showed in Figures 4 and 5. The influence of the iron oxide type on the processing temperature, when combined with the same metal organic reagent, is represented by a single plot. The impact of the organometallic reagent on the completion of the solid-state reaction is studied by comparing the various plots. Reported temperatures for nickel ferrite preparation using the conventional method range from 1100 to 1200°C. The modified powder process allows one to obtain nickel ferrites at temperatures comprised between 860 and 1100°C. In the same fashion, zinc ferrites are prepared at temperatures as low as 750°C and up to 900°C, which is considerably lower than the 1000 to 1100°C necessary for their conventional synthesis from metal oxide

powders. The gap between processing temperatures for complete nickel and zinc ferrite formations is accounted for by the difference in activation energies of the cation diffusion process, which was established to be the rate-controlling step of ferrite solid-state reactions³⁵. The reported activation enthalpies for NiFe₂O₄ and ZnFe₂O₄ formation were 120 kcal/mol and 80 kcal/Mol respectively.

- Iron Oxide Dependence on the NiFe₂O₄ Processing Temperature:

The plots of nickel metalorganic salts in Figure 4 show a common drop in processing temperatures when combined with γ -Fe₂O₃ instead of α -Fe₂O₃, with a slightly sharper decrease in the case of Ni(acetate)₂. Two aspects of the reaction must be considered to account for this trend: first, the thermal behavior of γ -Fe₂O₃ and, second, the microstructural properties of each starting metal oxide powder. The α structure is the thermally stable form of iron oxide, and exposure of the metastable γ -phase to heat results in its irreversible transformation into α -Fe₂O₃, usually at temperatures ranging from 400 to 550 °C, depending on the microstructural properties³⁶. The starting γ -phase possesses an inverse spinel structure with lattice parameter $a=8.352 \text{ \AA}$, and consists of face centered cubic (fcc) stacking of O²⁻ and random distribution of Fe³⁺ in both octahedral and tetrahedral sites along with a high concentration of cation vacancies³⁷. Investigation of the nature of the γ to α phase conversion revealed the transformation takes place along the [110] direction of the spinel lattice in a topotatic fashion and is accompanied by the restacking of O²⁻ from fcc to hcp ionic arrangement ($a=5.035 \text{ \AA}$, $c=13.75 \text{ \AA}$)³⁸. Phase transformations are characterized by an increase in reactivity and are therefore more favorable to chemical reactions with surrounding metal oxide particles, which results in early ferrite nucleation³⁹. Previous studies on the comparison of the preparation of

ferrites with α and γ iron oxides reported lower sintering temperatures and increased rates of “ferritization” when the γ form was employed⁴⁰⁻⁴²; the effect of the structure of f

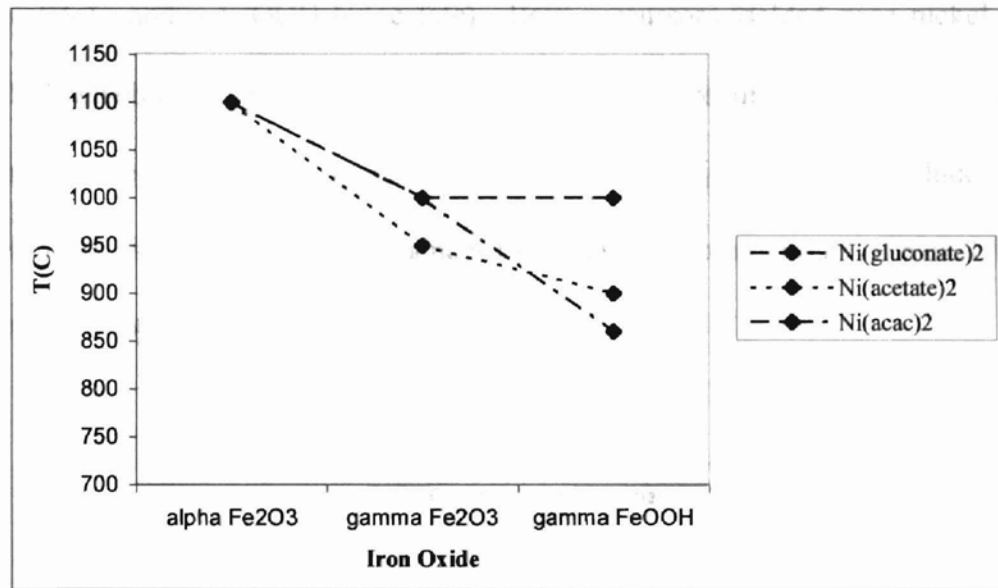


Figure 4. Nickel Ferrite Processing Temperatures

Microstructure is an essential factor in the improvement of reactivity of the starting metal oxide powders. For example, smaller particles have high surface energy, and are characterized by a low particle volume:particle surface ratio, they spontaneously attempt to minimize the latter by reacting with surrounding material and thereby increase their volume:surface ratio. Surface area measurements allow one to estimate the specimen grain size, hence the reactivity, and the surface available for NiO deposition around the iron oxide particles. The surface areas of the iron oxide powders investigated are listed in Table 4. The surface area measurements are in good agreement with the trends observed in Figure 4 where the processing temperature drops more or less sharply for each nickel precursor in the series α -Fe₂O₃, γ -Fe₂O₃, γ -FeOOH. The values reported in Table 4

suggest the particle size of gamma iron oxide is considerably smaller than that of the alpha iron oxide powder. In order to properly estimate the effect of the structure of Fe_2O_3 the formation temperature, NiFe_2O_4 was prepared with $\alpha\text{-Fe}_2\text{O}_3$ nanoparticles and $\text{Ni}(\text{acetate})_2$, and $\alpha\text{-FeOOH-Ni}(\text{acetate})_2$. Both precursors yielded pure nickel ferrite at 1000°C , which is slightly lower than the 900 and 950°C required for trevorite preparation from the $\gamma\text{-Fe}_2\text{O}_3\text{-Ni}(\text{acetate})_2$ and $\gamma\text{-FeOOH-Ni}(\text{acetate})_2$. It can be concluded that the choice of the iron oxide phase influences the completion temperature of nickel ferrite but to a rather small extent.

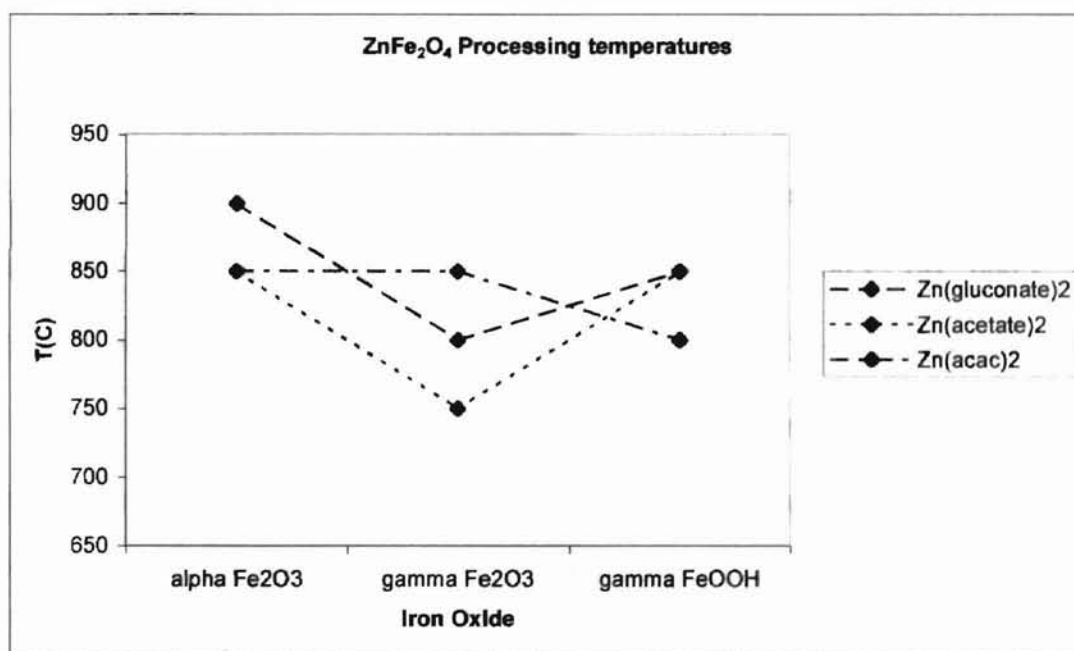


Figure 5. Processing Temperatures of ZnFe_2O_4 ($^\circ\text{C}$)

On the other hand, the zinc ferrite plots of total conversion temperatures versus iron oxide source (see Figure 5) do not display the same characteristics as those of nickel ferrite. If all three plots are considered, no clear pattern is discernable. Zinc gluconate and

zinc acetate precursors have lower formation temperatures when pyrolyzed with $\gamma\text{-Fe}_2\text{O}_3$, whereas no coherent dependence on the iron oxide form is observed in the case of zinc acetylacetonate precursors.

Table 4. Iron Oxide Powder Surface Area Measurements:

Iron Oxide powder	Surface area (m^2/g)
$\gamma\text{-Fe}_2\text{O}_3$	83.2
$\alpha\text{-Fe}_2\text{O}_3$	15.4
$\gamma\text{-FeOOH}$	183.3
$\alpha\text{-FeOOH}$	62.0

4. X-ray Study of Nickel Ferrite Formation:

Figure 6 shows the X-ray diffraction patterns of the products obtained by heating the $\text{Ni}(\text{acac})_2\text{-}\gamma\text{-Fe}_2\text{O}_3$ precursor at three different temperatures: 300°C (a), 600°C (b), 1000°C (c). NiO (a), $\gamma\text{-Fe}_2\text{O}_3$ (b), $\alpha\text{-Fe}_2\text{O}_3$ (c), and NiFe_2O_4 (d) X-ray patterns are shown in Figure 7. The removal of the acetylacetonate ligands occurs gradually over a wide temperature range, as shown in the TGA diagram Figure 8, and is fairly complete by 350°C. The initial weight loss is attributed to the evaporation of the water of hydration and of N,N dimethylformamide. The pyrolysis of Zinc and iron(III) acetylacetonates have been thoroughly investigated^{43,44}, and presumably, that of $\text{Ni}(\text{acac})_2$ is similar. It was demonstrated that both acac salts undergo the same decomposition reactions but at different temperatures. The first step following release of the coordination water results in the formation of the metal acetate with evolution of propyne⁴³. Partial combustion of the acetate ligands occurs at 300°C with release of acetone vapor, and formation of a

solid phase consisting of a metal oxide-metal carbonate mixed phase isomorphous to the corresponding metal oxide. The decomposition then goes to completion upon release of carbon dioxide gas over a wide temperature range extending up to 600°C. The TG/DTA study of $\text{Ni}(\text{acac})_2$ showed the decomposition was complete by 300°C and was then followed by a slight weight gain of 1.9% attributed to nickel metal oxidation to metal oxide. This was confirmed by the precursor powder pattern at 300°C where the characteristic peaks of nickel oxide and nickel metal ($2\theta = 44.5$ and 51.9) were identified.

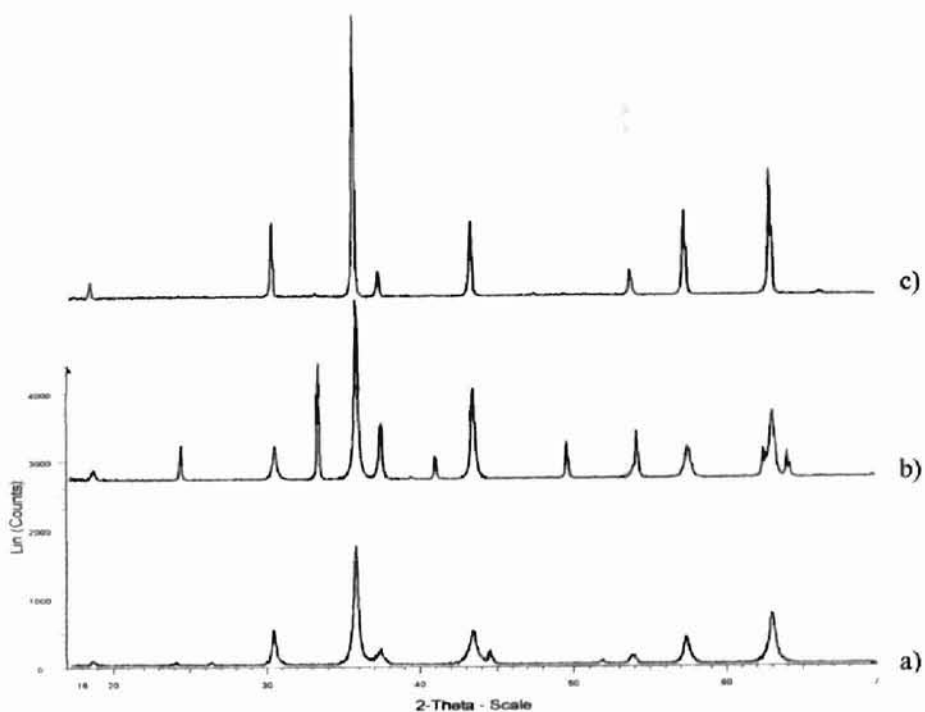


Figure 6. XRD of $\text{Ni}(\text{acac})_2\text{-}\gamma\text{-Fe}_2\text{O}_3$ Pyrolyzed at 300°C (a), 600°C (b) and 1000°C (c)

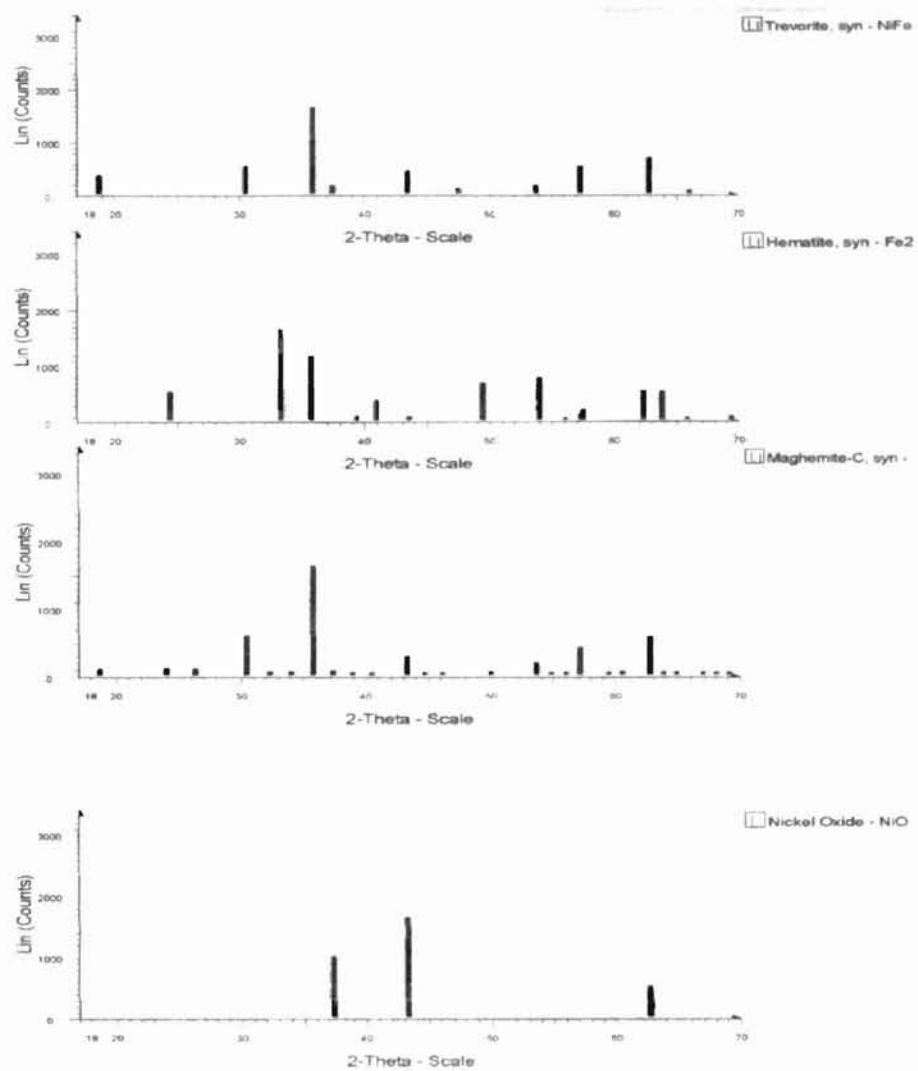


Figure 7. XRD Patterns of NiO, γ -Fe₂O₃ (Maghemite), α -Fe₂O₃ (Hematite), NiFe₂O₄ (Trevorite).

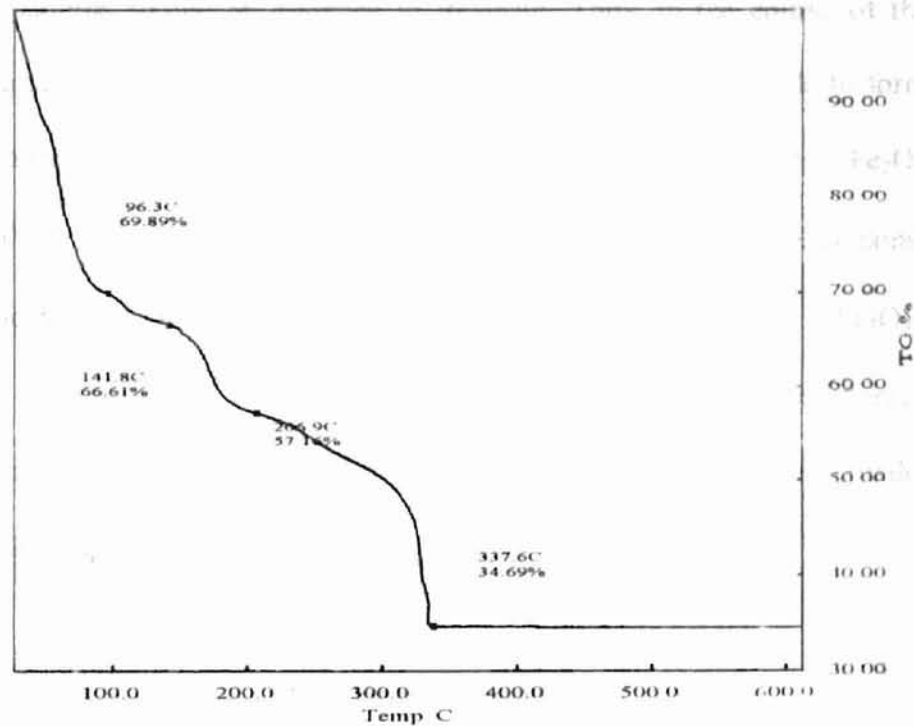


Figure 8. TGA of NiFe₂O₄ Precursor Ni(acac)₂-γ-Fe₂O₃

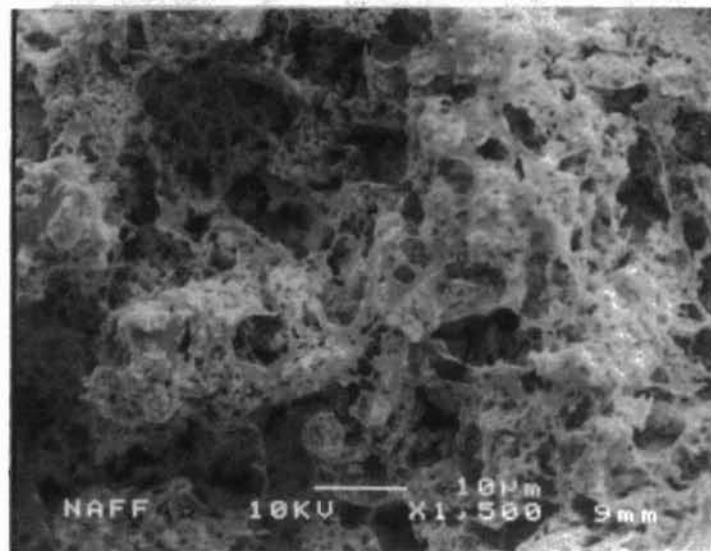
Due to a significant overlapping of NiFe₂O₄, trevorite, and γ-Fe₂O₃ (maghemite) powder patterns (see Figure 7), the X-ray patterns of Ni(acac)₂-γ-Fe₂O₃ at 300°C and 1000°C are almost identical, and evaluation of the solid-state reaction progression at 300°C is impossible. An X-ray diffraction study of the γ to α-Fe₂O₃ transformation revealed the structural conversion started at 400°C and was complete by 550°C (powder patterns not shown). The existence of intense hematite (α-Fe₂O₃) peaks in the precursor diffraction pattern at 600°C (Fig. 6 (b)) confirms the iron oxide phase conversion took place, and was unaffected by the presence of nickel oxide. This suggests that all of the iron oxide present in the sample at this stage of the reaction is in the alpha form. Therefore, it may be concluded that the set of peaks which match both NiFe₂O₄ and

maghemite patterns should be assigned to trevorite. Thus, in the course of the phase transformation, a fraction of the iron oxide has reacted with nickel oxide to form nickel ferrite. Comparison of the NiFe_2O_4 peak intensities on the $\text{Ni}(\text{acac})_2\text{-}\gamma\text{-Fe}_2\text{O}_3$ X-ray pattern at 600°C with that of $\text{Ni}(\text{acac})_2\text{-}\alpha\text{-Fe}_2\text{O}_3$ at the same temperature, demonstrated a more advanced stage of the nickel ferrite formation in the latter. The $\gamma\text{-Fe}_2\text{O}_3$ smaller particle size is an important factor in the nucleation step of solid state-reactions, and the fact that $\gamma\text{-Fe}_2\text{O}_3$ powder has a higher surface area than the $\alpha\text{-Fe}_2\text{O}_3$ powder could account for the improved NiFe_2O_4 growth.

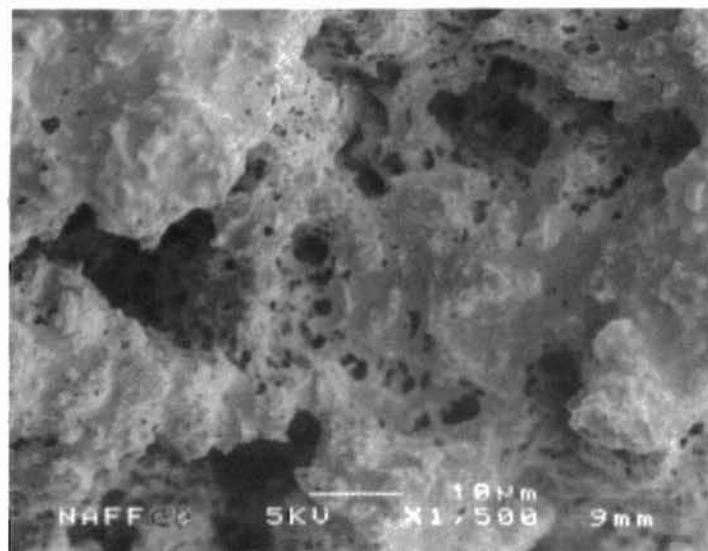
5. Morphology Study of the Metal Ferrite Powders:

The SEM micrographs of $\text{Ni}(\text{acetate})_2\text{-}\gamma\text{-Fe}_2\text{O}_3$ at 450°C (a) and 850°C (b) shown in Figure 9 provide a good illustration of the modified powder process. The starting γ iron oxide is a fine powder with particle size in the 80-90 nm as determined by SEM microscopy (Figure 10). After $\text{Ni}(\text{acetate})_2$ is coated onto the iron powder and decomposes at 450°C , a solid is created that is composed of what appears to be smooth nickel oxide films with embedded iron oxide grains (Figure 9 (a)). When the mixture is heated to 850°C and it converts to nickel ferrite, the resulting solid still maintains a sheet-like appearance but has become significantly more porous. There are large micron-sized pores similar to those present at 450°C but there are also numerous smaller pores that approximate the size of the original iron particles. As a result of the macroporous nature of the nickel ferrite product, it still maintains a significant surface area of $14.3 \text{ m}^2/\text{g}$. In general sintering would be expected to lead to densification and collapse of porous networks. In fact this has occurred since the total surface area has dropped but this

appears to be due to the loss of small pores in the web-like strands of the final product. The opening of larger pores is the result of the mechanism of solid-state reaction between NiO and Fe₂O₃. In this reaction, NiFe₂O₄ forms at the interface between the nickel and iron oxide. Then subsequent formation of nickel ferrite occurs by diffusion of iron oxide through the nickel ferrite barrier film to the point where it can react with nickel oxide. Since nickel oxide does not diffuse inward, the result is an outward migration of iron. In the case of this precursor, the iron flows into the sheet-like networks of nickel oxide, leaving pores behind and generating a web-like morphology for the final product. The observed behavior is different than that of Ni(MEEA)₂ in which uniformly coated particles puffed into broccoli flower-like collection of small particles. Thus, it has been demonstrated that the morphology at the deposited nickel oxide, as controlled by the choice of nickel precursor, has a tremendous influence on the morphology of the final product.



b)



a)

Figure 9. SEM of $\text{Ni}(\text{acetate})_2\text{-}\gamma\text{-Fe}_2\text{O}_3$ Pyrolyzed at 450°C (a) and 800°C (b)

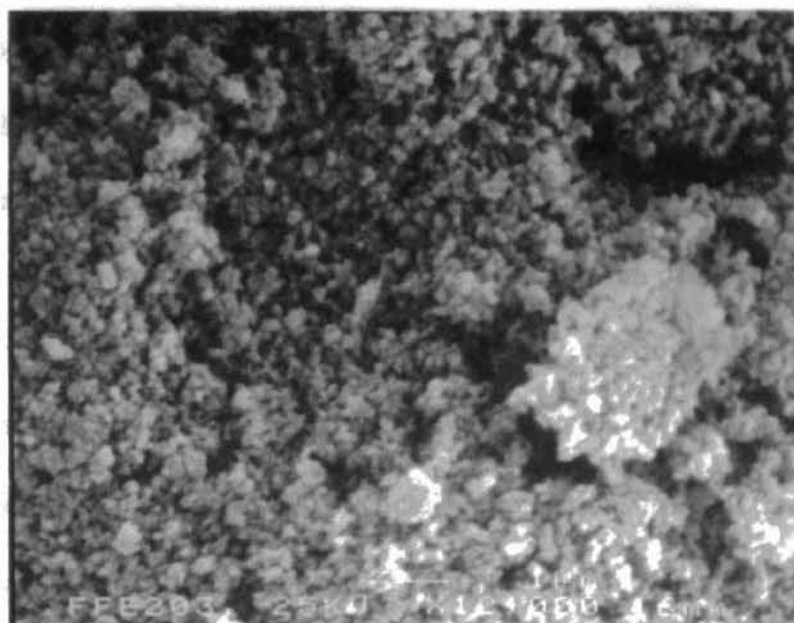
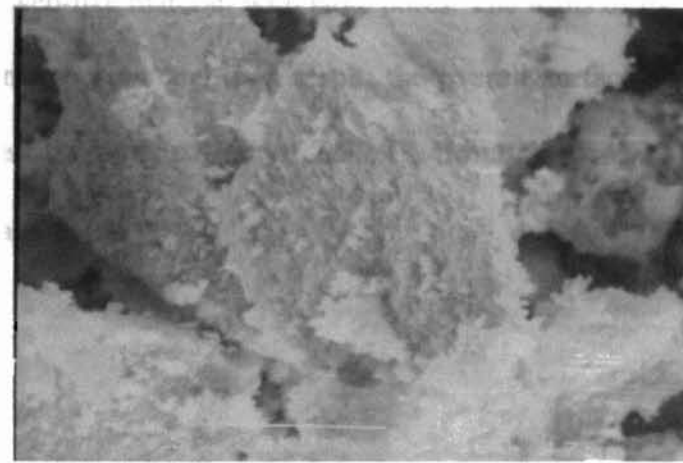


Figure 10. SEM of $\gamma\text{-Fe}_2\text{O}_3$ (x 12,000)

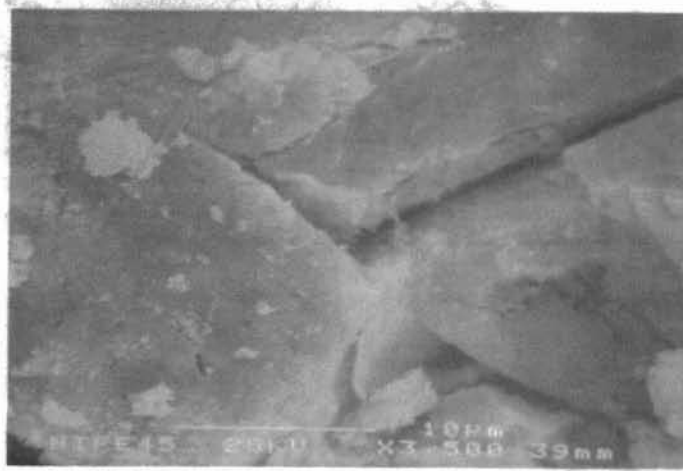
Thus, as expected, $\text{Ni}(\text{acac})_2$ produced more homogeneous coating of nickel oxide. The SEM images of $\text{Ni}(\text{acac})_2\text{-}\gamma\text{-Fe}_2\text{O}_3$ pyrolyzed at 130°C (a), 450°C (b), and 1000°C (c) are shown in Figure 11. Crystals of dehydrated $\text{Ni}(\text{acac})_2$ are clearly visible (Figure 11(a)) and cover much of the iron oxide particles so that the latter may be described as embedded within the crystals. The intervention of an intermediate phase such as the $\text{Ni}(\text{acac})_2$ melt at 230°C, resulted in a very homogeneous solid with highly uniform flat surfaces. Subsequent thermal treatment to 450°C caused the structure to densify, and produce a very compact material mostly consisting of NiO , and $\gamma\text{-Fe}_2\text{O}_3$ as evidenced by the X-ray pattern. Presumably the temperature gap between the melting point and the decomposition temperature allowed for $\text{Ni}(\text{acac})_2$ to uniformly diffuse and deposit on the iron particles before decomposing to nickel oxide. Sintering to 1000°C resulted in a very

fine powder of crystallite and particle sizes of 48.9 nm and 250 nm, and lower porosity than Ni(acetate)₂- γ -Fe₂O₃. However, the morphology of the final ferrite was completely different than that from the Ni(MEEA)₂ experiments¹⁵ since this product consists of micron-sized grains of nickel ferrite (see Figure 11 (b)). The difference between the two procedures may arise from difference in the extent of nucleation of nickel ferrite. In the case of Ni(MEEA)₂ no intermediate formation of NiFe₂O₄ was observed before a very abrupt transition from a NiO- α -Fe₂O₃ mixture to NiFe₂O₄. On the other hand, the XRD pattern of the Ni(acac)₂ precursor at 600°C contained reflections from all three crystalline phases. The cause of this difference might be attributed to two separate phenomena, one physical and one chemical. As previously demonstrated, the phase transition from γ to α -Fe₂O₃ can influence nucleation of NiFe₂O₄ if nickel ions were migrated into lattice positions that were being vacated by ferric ions. If this were the case, the Ni(MEEA)₂ experiments which were performed with α -Fe₂O₃ would not have benefited from this phase transition. Secondly, Baron *et al.* have demonstrated the metal acetylacetonates can undergo metal ion exchange with aluminum-oxygen polymers, producing Al(acac)₃ and substituting a new metal with the metal oxide backbone⁴⁵. A similar phenomenon in the Ni(acac)₂- γ -Fe₂O₃ mixture would lead to significant mixing of iron and nickel and the surface of the iron oxide and promote nucleation of NiFe₂O₄.

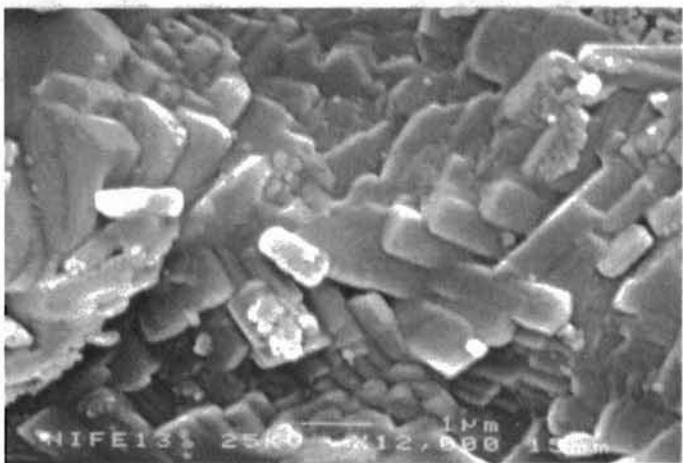
The use of metal gluconates as the oxide coating source led to yet another morphology. Gluconate salts tend to caramelize upon heating in a similar fashion to glucose from which it is derived. Dehydration and combustion of this sticky intermediate leads to an expanded foamy solid. The morphology of the resulting ferrites (see Figure



c)



b)



a)

Figure 11. SEM of $\text{Ni}(\text{acac})_2\text{-}\gamma\text{-Fe}_2\text{O}_3$ Precursor Pyrolyzed at 130°C (a), 450°C (b), and 1000°C (c).

12) is a tortuous web-like material with large pores. The walls of the metal oxide network appeared to be non porous and as a result, the overall surface area is low. Figure 13 shows a characteristic X-ray pattern of $ZnFe_2O_4$ from the pyrolysis of $Zn(gluconate)_2 \cdot \gamma\text{-Fe}_2O_3$ at 600°C and 850°C .

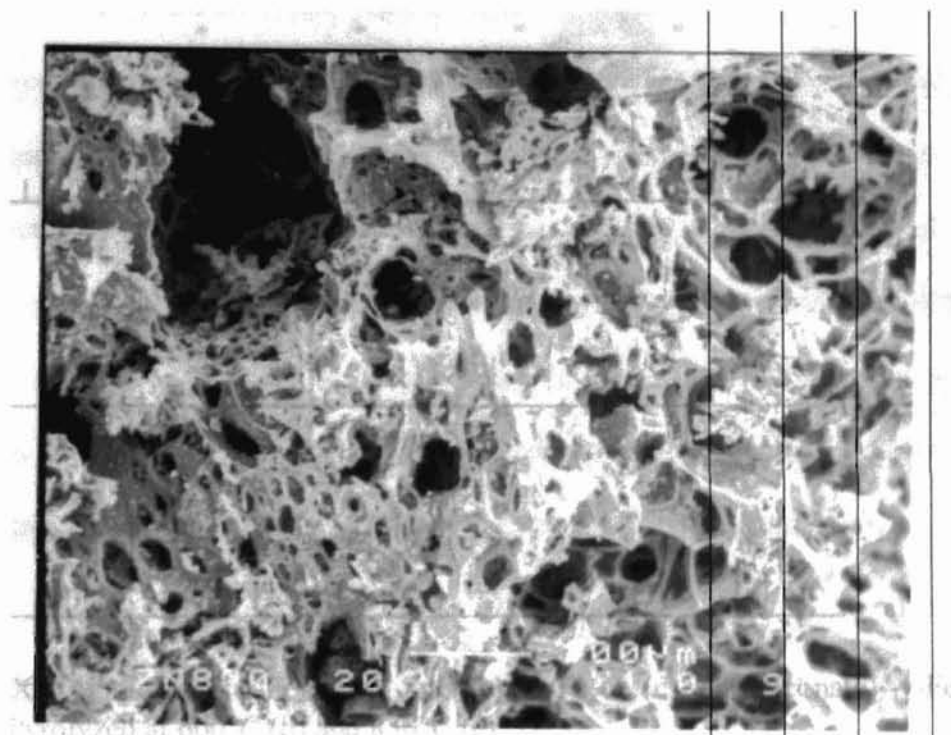


Figure 12. SEM of $Zn(gluconate)_2 \cdot \gamma\text{-Fe}_2O_3$ Precursor Pyrolyzed at 850°C

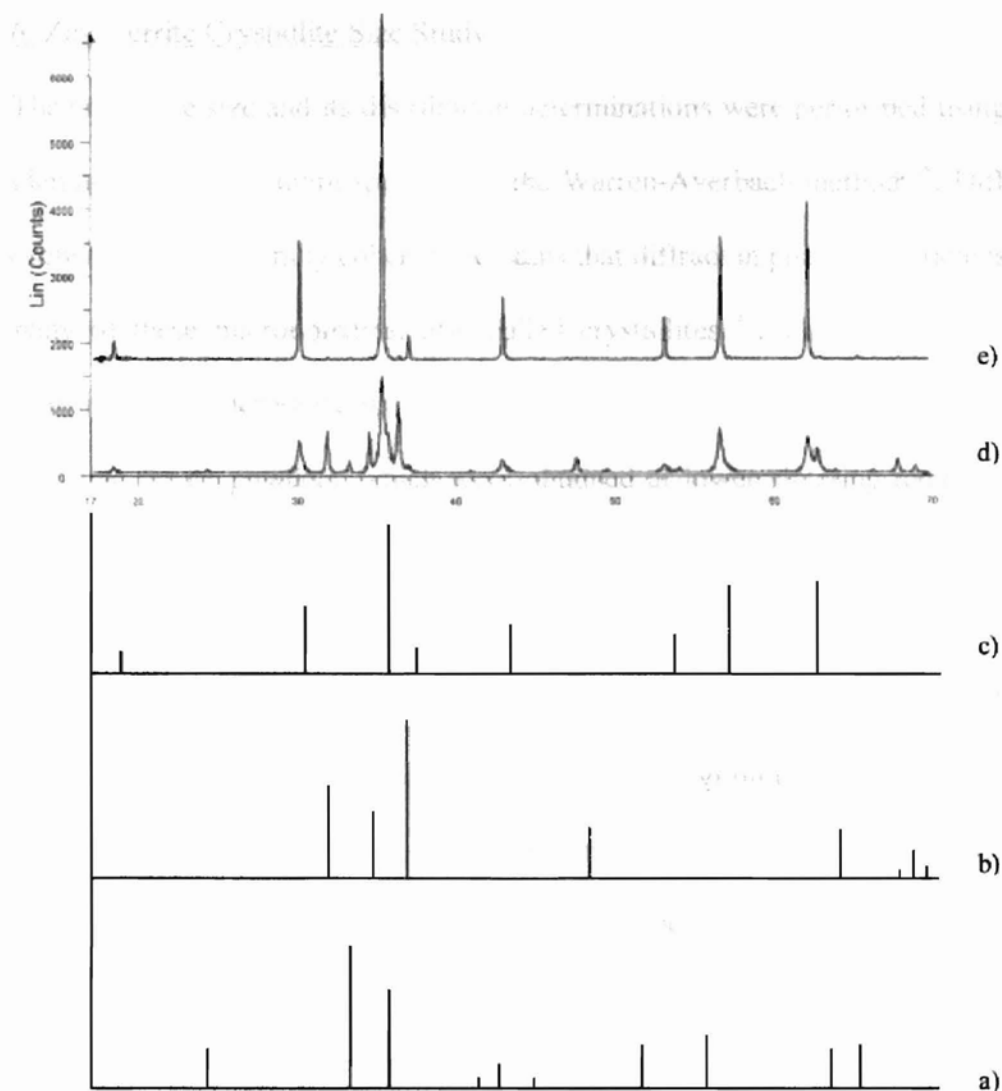


Figure 13. XRD Patterns of α -Fe₂O₃ (a), ZnO (b), ZnFe₂O₄ (c), Zn(gluconate)₂- γ -Fe₂O₃ Pyrolyzed at 600°C (d) and 850°C (e),

Precursors containing α or γ iron oxyhydroxide did not exhibit morphological features particularly different from the samples containing iron oxide. Although the particle and crystallite sizes did change with the nature of the iron source, the morphology seemed to be more dependent on the metal ligand type.

6. Zinc Ferrite Crystallite Size Study:

The crystallite size and its distribution determinations were performed using the peak broadening theory, and more specifically the Warren-Averbach method⁴⁶. Diffraction is only sensitive to structurally coherent domains that diffract in phase; a particle is made up of many of these microdomains, also called crystallites⁴⁷. The crystallite size is the average size of all microdomains⁴⁸.

The zinc ferrite powders, which were obtained at lower sintering temperatures than NiFe_2O_4 , were selected for a crystallite size study, which aims at demonstrating the strong influence of the nature of the precursor on the microstructural properties of the final product. A similar comparison could not be made in the case of nickel ferrite because some of the products had undergone extensive grain growth and did not display broadened X-ray reflections. The clear dependence of the ferrite crystallite size with the precursor is illustrated in Figure 14. Each experimental point represents a precursor whose sintered zinc ferrite has the crystallite size indicated on the abscissa.

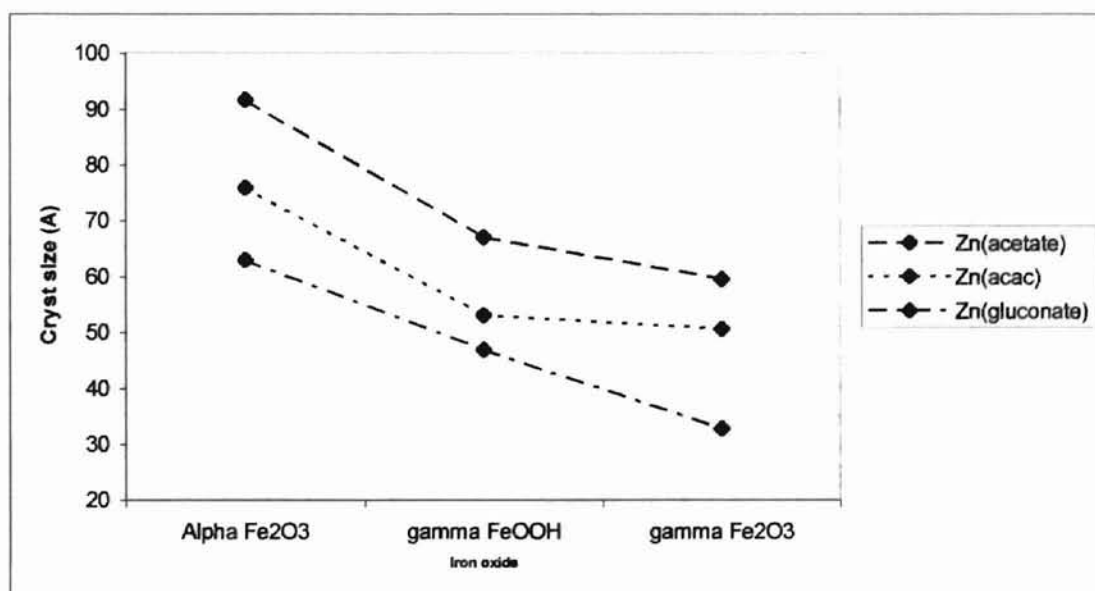


Figure 14. ZnFe_2O_4 Crystallite Size Measurements Using Line-broadening Method

The nature of the metalorganic compound not only influences the morphology of the product but it also has a dramatic effect on the microstructural properties of the ferrites. There is a consistent decrease in final crystallite size in the sequence of the acetate, acac, and gluconate ligands. It should be noted the same trend is observed for each category of iron oxide, and it is in agreement with the crystallite size and surface area measurements listed in Table 5. The latter were performed after pyrolysis at 450°C of the various zinc compounds, this temperature being approximately that of ferrite nucleation. Although one material may possess a lower crystallite size than another, this does not mean its grain, or particle, size follows the same tendency. Surface area measurements, which are more representative of the sample particle size, allowed us to examine the particle size trend of the ZnO precursors, which was confirmed to be the same as that of crystallite size^{49,50}. In addition to the ferrite crystallite size dependence on the zinc ligand type, there is also good agreement between the zinc oxide and zinc ferrite surface areas listed in Table 6. The agglomeration process leading to particle growth is specific to each zinc precursor. It can be concluded that the particle and crystallite growth patterns of the zinc oxide precursors are retained when combined with iron oxide powder in ferrite synthesis.

Table 5. Crystallite Size and Surface Area Measurements of Zinc Precursors Pyrolyzed at 450°C

Zinc precursor	Surface area (m ² /g)	Crystallite size (Å)
Zn(gluconate) ₂	19.8	16
Zn(acac) ₂	10.1	22.3
Zn(acetate) ₂	7.9	31.6

The iron oxide form affected the final crystallite size in a less consistent fashion. The crystallite sizes of ferrites from the precursors containing zinc gluconate decreased sharply when changing from pure Fe_2O_3 , to $\gamma\text{-FeOOH}$, to $\gamma\text{-Fe}_2\text{O}_3$, which is consistent with the iron oxide surface area measurements listed in Table 4. However it appears that for the ferrites with larger sizes, i.e. from zinc acetate and zinc acac precursors, the difference between the γ -oxyhydroxide and iron oxide samples is greatly attenuated. Several factors have to be considered to account for this phenomenon. First, the surface area measurements of $\gamma\text{-FeOOH}$ and $\gamma\text{-Fe}_2\text{O}_3$ at 450°C reveal a sharp drop from 183.2 to $55.4 \text{ m}^2/\text{g}$ for the oxyhydroxide, while the fine iron oxide powder only decreased from 83.2 to $47.5 \text{ m}^2/\text{g}$. Therefore, the heat treatment greatly diminished the initial S_A gap determined between the two powders at room temperature. However, this effect is only noticeable for precursors with large crystallite size, (i.e. $\text{Zn}(\text{acac})_2$ and $\text{Zn}(\text{acetate})_2$). Secondly, the sintering temperature is of great importance when analyzing the ferrite crystallite size.

Table 6. Zinc Ferrite Surface Area at Reaction Completion Temperature (m^2/g) :

Precursor	Sintering Temperature	Surface Area	Surface Area at 800°C
$\text{Zn}(\text{gluconate})_2 - \gamma \text{Fe}_2\text{O}_3$	800	25.9	25.9
$\text{Zn}(\text{acac})_2 - \gamma \text{Fe}_2\text{O}_3$	850	20.3	24.3
$\text{Zn}(\text{acetate})_2 - \gamma \text{Fe}_2\text{O}_3$	750	10.0	9.7
$\text{Zn}(\text{gluconate})_2 - \gamma \text{FeOOH}$	850	6.56	6.02
$\text{Zn}(\text{acac})_2 - \gamma \text{FeOOH}$	800	3.40	3.40
$\text{Zn}(\text{acetate})_2 - \gamma \text{FeOOH}$	850	3.05	3.42

High temperature treatments result in the reduction of grain interfaces and therefore promote the crystallite and particle growth. $\text{Zn}(\text{acac})_2\text{-}\gamma\text{-Fe}_2\text{O}_3$ has a final sintering temperature 100°C higher than that of $\text{Zn}(\text{acetate})_2\text{-}\gamma\text{-Fe}_2\text{O}_3$, and 50°C above that of $\text{Zn}(\text{gluconate})_2\text{-}\gamma\text{-Fe}_2\text{O}_3$. This would account for the unusually high $\text{Zn}(\text{acac})_2\text{-}\gamma\text{-Fe}_2\text{O}_3$ crystallite size which causes the $\text{Zn}(\text{acac})_2$ plot of Figure 14 to deviate strongly from a regular drop.

Crystallite Size Distribution:

Regardless of the compound of interest, as the average crystallite size decreases the crystallite size (C.S.) distribution plot flattens, mostly caused by an irregular agglomeration process. For example, of all the zinc oxides obtained from pyrolysis of the zinc metalorganic compounds described earlier, $\text{Zn}(\text{gluconate})_2$ has the narrowest crystallite size distribution, plotted in Figure 15. These results are consistent with the experimental data in Table 9. This effect is also quite noticeable in the C. S. distributions of the three zinc ferrite powders prepared with $\gamma\text{-Fe}_2\text{O}_3$, shown in Figure 16 and the C.S. distributions of the zinc ferrites from $\text{Zn}(\text{gluconate})_2$ precursors. The dependence on the iron oxide form is also illustrated in Figure 17.

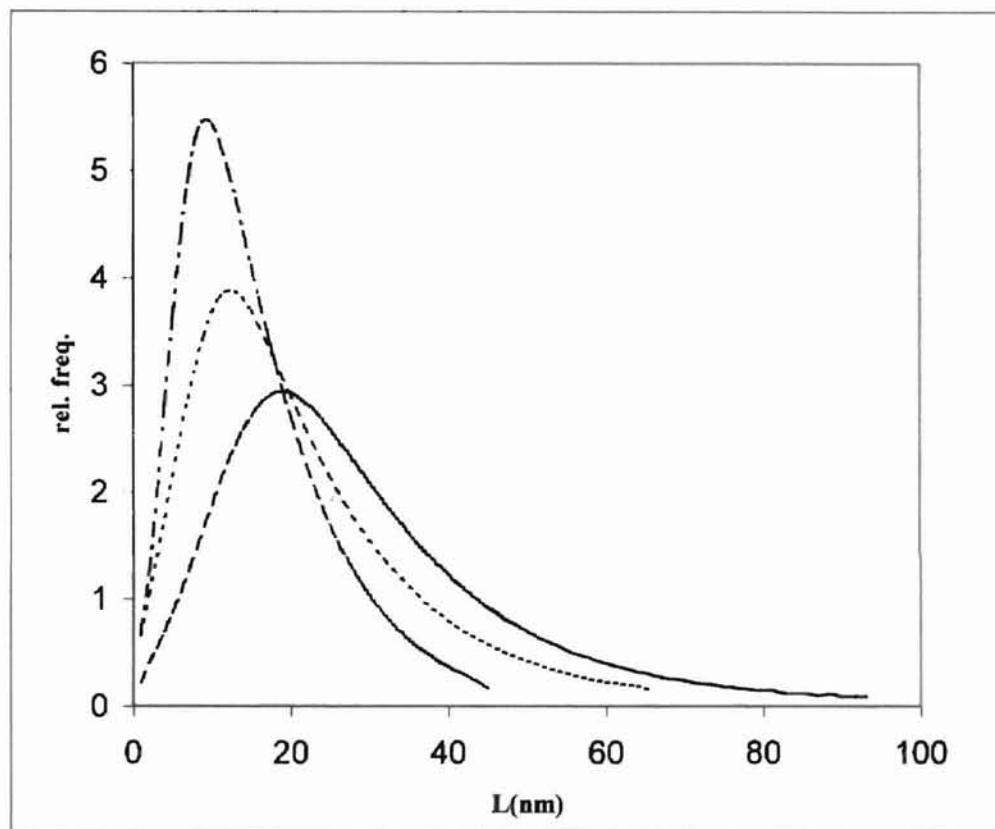


Figure 15. Crystallite Size Distributions of $\text{Zn}(\text{gluconate})_2$ (---), $\text{Zn}(\text{acac})_2$ (---), $\text{Zn}(\text{acetate})_2$ (—) samples pyrolyzed at 450°C .

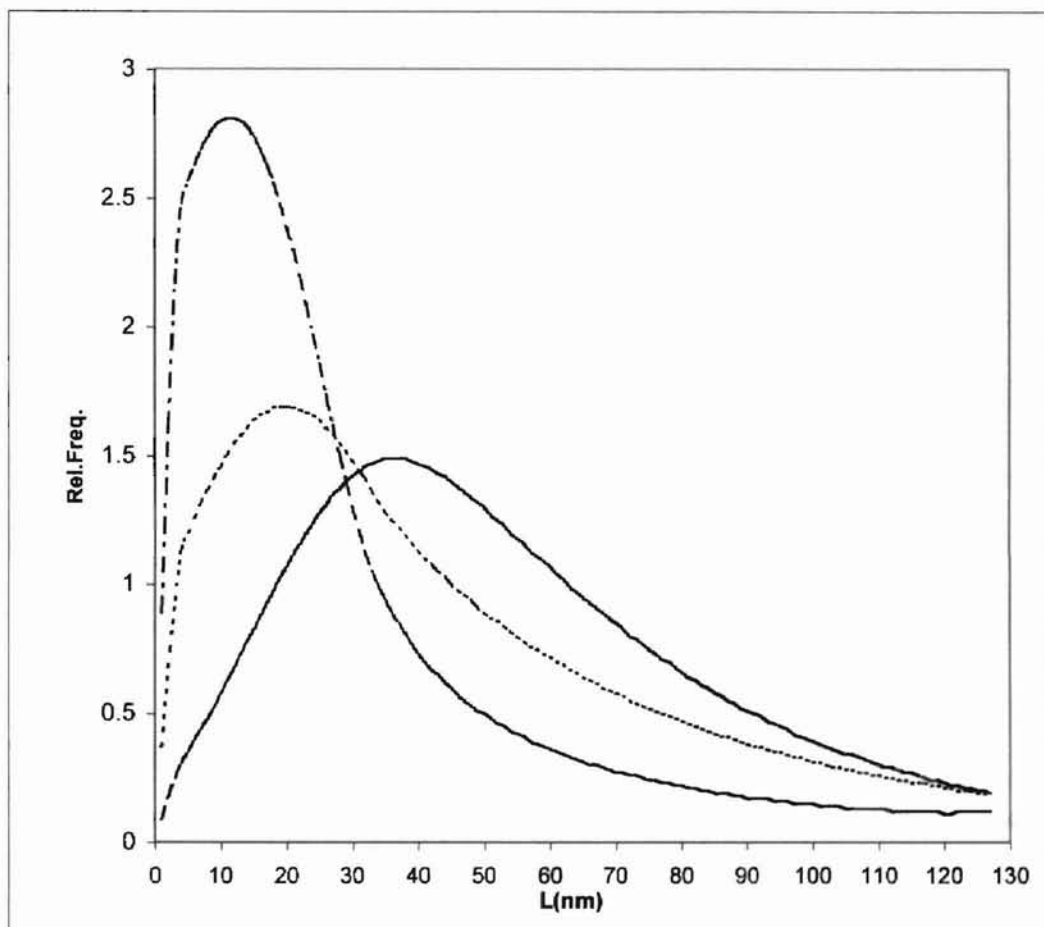


Figure 16. Crystallite Size Distributions of ZnFe_2O_4 from $\text{Zn}(\text{gluconate})_2\text{-}\gamma\text{-Fe}_2\text{O}_3$ (— — —), $\text{Zn}(\text{acac})_2\text{-}\gamma\text{-Fe}_2\text{O}_3$ (· · ·), and $\text{Zn}(\text{Acetate})_2\text{-}\gamma\text{-Fe}_2\text{O}_3$ (— — —) Precursors.

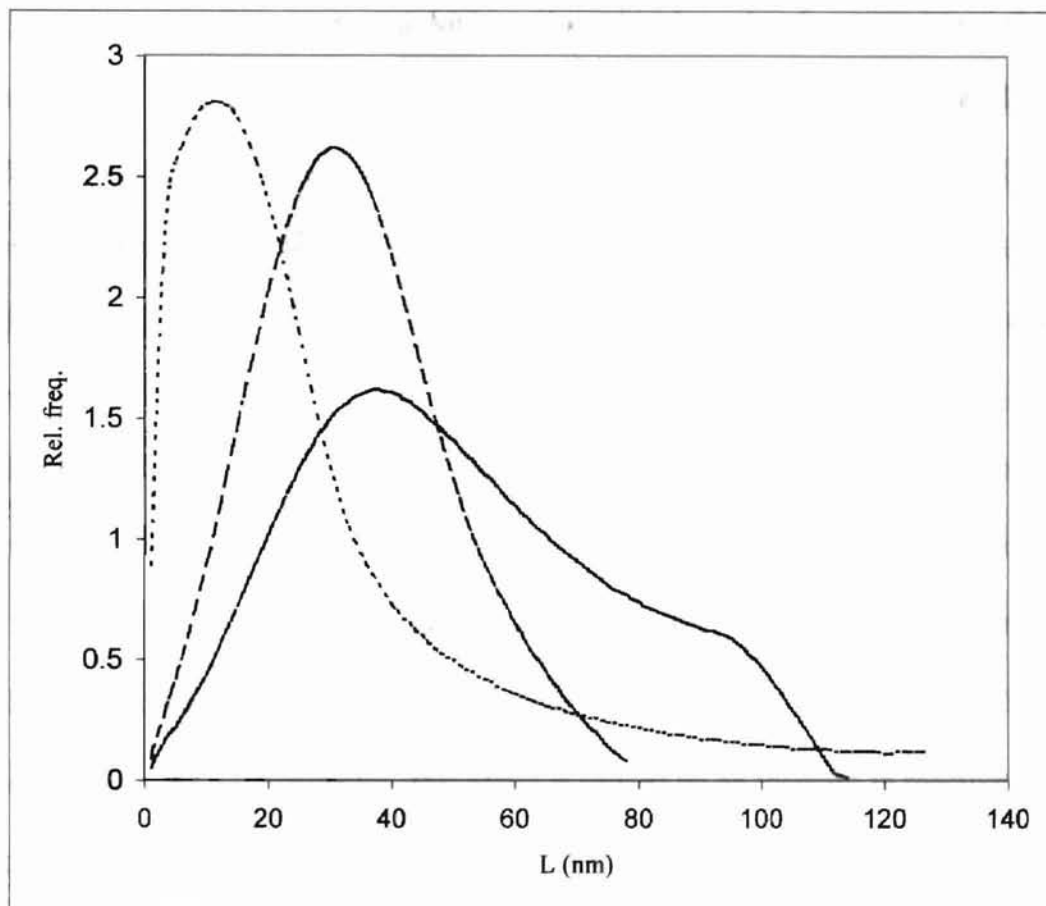


Figure 17. Crystallite Size Distributions of Zinc Ferrite from the $\text{Zn}(\text{gluc})_2\text{-}\gamma\text{Fe}_2\text{O}_3$ (---), $\text{Zn}(\text{gluc})_2\text{-}\alpha\text{Fe}_2\text{O}_3$ (- · -), and $\text{Zn}(\text{gluc})_2\text{-}\gamma\text{FeOOH}$ (—) Precursors

7. Conclusion:

A new economic method, the modified powder process, was developed for the synthesis of an important class of metal oxide ceramic: the ferrites. This new technique, which allows the synthesis of nickel and zinc ferrites at temperatures as low as 750°C, is based on the pyrolysis of a precursor consisting of a fine iron oxide powder combined with an organometallic compound $M(L)_2$. Upon heating, the decomposition of $M(L)_2$ leads to the coating of the iron oxide particles with the corresponding metal(II) oxide, resulting in an highly stoichiometric homogeneous mixture of Fe_2O_3 and $M(II)O$. Based on previous studies and the final ferrite powder morphologies, it was concluded that the solid-state mechanism following MFe_2O_4 nucleation takes place through diffusion of iron oxide through the ferrite phase to react with the outer layer of metal oxide.

The iron oxide phase was shown to have a slight influence on the final sintering temperature. For α and γ iron oxide powders of similar particle size the ferrite nucleation was found to occur at lower temperatures for the precursor $Ni(\text{acetate})_2\text{-}\gamma\text{-}Fe_2O_3$ and resulted in reaction completion at 900°C, while pure ferrite was obtained at 1000°C from $Ni(\text{acetate})_2\text{-}\alpha\text{-}Fe_2O_3$. Presumably, this effect is caused by an increase in reactivity during the phase conversion of gamma iron oxide to the alpha structure throughout the 450 to 550 temperature range. The microstructure of the ferrite powder was not affected by the nature of the iron oxide powder phase.

The coordination compounds investigated in the present study were the nickel and zinc acetates, gluconates, and acetylacetonates. The nature of the organic ligand did not affect the final processing temperature to a great extent, however it was demonstrated it is a determinant factor when considering the morphology of the ferrite powder. For

example, pyrolysis of the NiFe_2O_4 precursor $\text{Ni}(\text{acetate})_2\text{-}\gamma\text{-Fe}_2\text{O}_3$ produced a web-like material with large pores with high surface area, whereas the thermal decomposition of $\text{Ni}(\text{acac})_2\text{-}\gamma\text{-Fe}_2\text{O}_3$ resulted in a pore free very fine material. Crystallite size study from X-ray line broadening theory of the metal oxide reactants and metal ferrite confirms the strong correlation between the sintered product and its reactants, the ferrite was shown to retain the microstructural characteristics of the initial precursor components.

The new modified powder process allows one to prepare low temperature ferrites with advanced microstructural features at a lower cost than most chemical techniques. Furthermore, the ferrite powder morphological characteristics can be tailored by using a specific metalorganic compound for precursor preparation. Further study of the modified powder process with a wider variety of coordination compounds would most likely result in the production of a range of metal oxide ceramics with diverse morphologies.

B. Ni(OH)₂ Solution growth process:

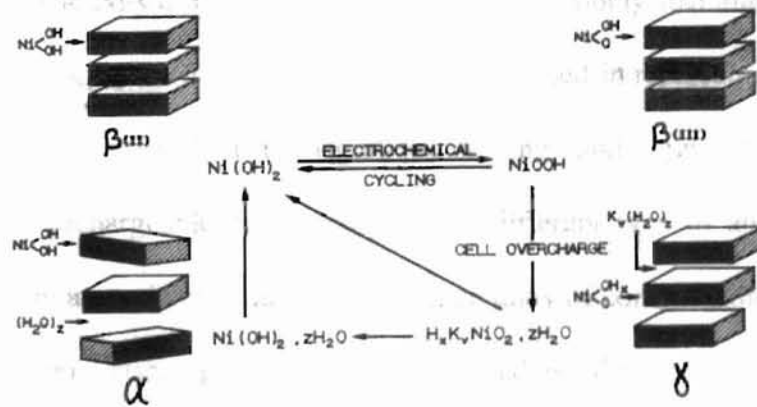
1. Introduction:

In the previous sections, it was shown that metalorganics are quite suitable for producing metal oxide coating in the modified powder process. The moderate cost of these reagents is offset by the ability to readily control the morphology of the final product. Nevertheless even more economical metal oxide precursors are desirable. Therefore, a solution growth process that could be used to coat iron oxide powders with nickel hydroxide was developed.

Nickel hydroxide can crystallize in two polymorphs: alpha and beta Ni(OH)₂. Both are described as layered structures, each layer consisting of NiO₂ slabs. The hydroxyl ions form a hexagonal close-packed structure with Ni(II) occupying octahedral interstices one plane out of two. The beta structure is the most stable and characterized by the absence of O-H bonding between adjacent layers, as evidenced by the strong narrow stretching vibration ν_{OH} band at 3600 cm⁻¹. The lattice parameters for β -Ni(OH)₂ in the hexagonal system are $a = 3.12 \text{ \AA}$ and $c = 4.605 \text{ \AA}$ (interlayer spacing)²⁴. On the other end, the α -Ni(OH)₂ structure (formula 2Ni(OH)₂.3H₂O), with interlayer spacing $c = 8.05 \text{ \AA}$, consists of parallel and equidistant Ni(OH)₂ layers randomly oriented and separated by intercalated water molecules hydrogen-bonded to the hydroxyl groups. In certain cases, protons, alkali ions and even anions can be reversibly intercalated and removed during electrochemical cycling. When immersed in alkaline environment, α -Ni(OH)₂ becomes unstable, and as the intercalated molecules are slowly eliminated and transforms into the beta phase²⁴.

Beyond the application as a source for a nickel oxide coating in the modified powder process, nickel hydroxide has numerous other applications, that could benefit from a process for generating Ni(OH)₂.

Nickel hydroxide has been extensively applied as active material for positive electrode of secondary alkaline batteries because of its remarkable cycling reversibility. During the oxidation process, β and α-Ni(OH)₂ are respectively converted to the β and γ NiOOH phases. The oxidation and reduction reactions involved are shown in Figure 18.



1: Charge 2: Discharge K: monovalent cation

Figure 18. Bode diagram ⁵²

On prolonged charging β-Ni(OH)₂ is converted to γ-NiOOH causing irreversible damage to the electrode due to the accompanying mechanical deformation ⁵³. On the contrary, α-Ni(OH)₂ is reversibly cycled to γ-NiOOH without any mechanical alteration.

Due to the alpha phase instability in alkaline environment, β-Ni(OH)₂ is frequently preferred for precursor material in alkaline batteries. The first nickel-based rechargeable

cell, invented by Thomas Edison in 1890, consisted of a nickel hydroxide cathode coupled with an iron anode and an alkaline electrolyte using potassium hydroxide (Ni / 2NiOOH / Fe). Despite a very long cycle life and robustness, the Ni/Fe alkaline cell suffers from deficiencies stemming from the iron electrode, which tends to undergo self-discharge on standing as a result of corrosion⁵⁴. The invention of this rechargeable nickel battery paved the way for the development of other types of nickel-based cells, the common nickel cadmium cell (Ni-Cd), the Ni-Zn cell, the Ni-hydrogen battery (aerospace batteries), and nickel metal hydride cells used for the powering of portable electronic devices such as the lap-top computers, wireless telephones and more recently electric vehicles. The Ni-Cd alkaline battery is the most widely manufactured despite a modest specific energy (30-40 Wh/kg). It is commonly used in replacement for lead/acid batteries in the automotive industry (ignition, starting, and lighting) and in certain airplanes. Ni-MH rechargeable cells incorporate a different type of anode that allows hydrogen storage in a specialized metal structure, an alloy of composition AB₅ (example: LaNi₅) or AB₂. Upon discharge, hydrogen is inserted within the alloy lattice without bonding to it, and is released during the charging process (see Equation 3 below). One drawback to the Ni-MH cell is rapid self-discharge, reliable means for hydrogen storage still needs to be found.



Ni-MH rechargeable battery: Anode reaction

In general, nickel-based batteries are excellent for applications that require rechargeable batteries that take very little time to recharge, and will survive under less than optimal conditions.

Nickel hydroxide electrode designs⁵⁵:

The active material in a Ni(OH)₂ electrode can be contained in nickel-plated steel strips crimped together to form pockets (*pocket plate cell*) commonly used in Cd/NiOOH batteries. Ni(OH)₂ can also be mixed with carbon, bonded by a polymer and rolled into sheets; this so-called *bonded electrode* is the cheapest but subsequent swelling during cycling causes irreversible damage. Finally, the highest quality nickel hydroxide electrode consists of a sponge-nickel plaque with Ni(OH)₂ filled-pores. This relatively expensive long-lasting electrode is mostly utilized in the aerospace industry.

Preparation Methods for Nickel Hydroxide:

The quality of a nickel-based positive electrode is directly dependent on the chemical and physical characteristics of the active material. In order to produce an electrode with high charge rate and good charge-discharge characteristics, Ni(OH)₂ needs to possess high surface area, narrow particle diameter distribution and a globular form (low crystallinity)⁵⁶.

- Electrosynthesis:

Electrosynthesized nickel hydroxide (ESN), designated as pure alpha Ni(OH)₂ with surface area 17 to 21 m²/g, was obtained by cathodic reduction of a nickel nitrate solution (pH=3.5) using a three electrode assembly⁵⁷. The electrogeneration of base through

nitrate ion reduction causes nickel hydroxide to slowly precipitate onto the platinum cathode. Nickel hydroxide prepared in this fashion possesses higher oxidizing power characterized by the excess charge on the nickel cation (+2.03) and formation of proton vacancies. These proton layer vacancies would account for the higher proton diffusion coefficient observed in ESN and for the faster kinetics of the α -Ni(OH)₂ to γ -NiOOH phase transition as compared to that for β -Ni(OH)₂ to β -NiOOH ²⁴.

- Precipitation methods:

Ni(OH)₂ precipitation usually takes place upon addition of a strong base (e.g. 1M potassium hydroxide) to a nickel nitrate solution ^{58, 59}. This preparation method yields beta nickel hydroxide with coarse particles having a diameter of 1 to several hundred μ m with irregular form and low density, and therefore undesirable for electrode application ⁵⁸. Micron-sized β -Ni(OH)₂ powder was obtained by converting nickel oxalate precipitate to Ni(OH)₂ in a sodium hydroxide solution ⁶⁰. A variation of the precipitation reaction consists of adding an excess of ammonia to a nickel salt solution. On boiling this solution, β -Ni(OH)₂ slowly precipitates from the Ni(II) hexa-ammine solution ⁶¹. The method can be used to prepare β nickel hydroxide having a high density but the lack of control over the deposition rate and the solution pH often results in irregular particle diameter distribution.

In order to prevent the transformation from β -NiOOH to γ -NiOOH during overcharging, elements such as Co, Zn, or Cd can be added in very small quantity to the nickel hexaammine solution. The hydroxides are then precipitated by injection of an

aqueous sodium hydroxide. The presence of these additives is thought to change the interlayer bonding forces of the nickel crystal lattice, through substitution of Ni ions with the element, thereby reducing the formation of γ -NiOOH⁶².

Stabilized alpha nickel hydroxide

Much effort has been devoted to developing processes that would slightly alter the chemical composition of alpha Ni(OH)₂ and stabilize its structure in alkaline medium. Compounds of formula Ni_(1-x)Al_x(OH)₂(CO₃)_{x/2}·0.66 H₂O, known as Ni-Al Layered Double Hydroxides (LDHs), have structural features very similar to those of α Ni(OH)₂. A stable aluminum-substituted alpha phase was synthesized by addition of NaOH to a solution containing the metal nitrates with ratio Ni:Al = 4:1 and sodium carbonate⁶³. The structure was retained upon aging in a 1M KOH solution for a month. The substitution of Ni(II) ions by Al(III) increases the number of intercalated anions to maintain the charge neutrality within the structure thereby enhancing the bonding strength between NiO slabs.

- Chimie douce process:

Another approach to nickel hydroxide and nickel oxyhydroxide synthesis consists of simultaneous exchange and intercalation reactions based on NaNiO₂, which exhibits the same typical NiO₂ slabs with smaller interlayer spacing $c = 5.2 \text{ \AA}$ ⁶⁴. Upon immersion in water, sodium nickelate exchanges intercalated Na⁺ for H₃O⁺, which leads to the release of OH⁻. Depending on the solution pH, the amount of H₃O⁺ inserted varies: Acidic pHs favor the formation of β Ni(III)OOH by promoting complete removal of Na⁺ and H₂O molecules. On the other hand, the insertion of hydronium ions at neutral pH generates a

layered phase with interlayer spacing approaching that of γ NiOOH-Na \cdot zH₂O ($c \approx 7\text{\AA}$). No hydrolysis reaction was observed in basic medium. Alpha-Ni(OH)₂ is obtained by reducing the Ni ion from oxidation state ≥ 3 to 2 using hydrogen peroxide as a reducing agent. Stabilization of this α -type phase in basic medium was achieved by partial substitution of nickel with cobalt using a solid solution with formula NaCo_xNi_(1-x)O₂ as starting reagent.

Solution growth also known as chemical bath deposition is a promising alternative to metallorganic deposition for the preparation of metal oxide coatings such as those used in the modified powder process. The typical solution growth process cannot be used for deposition of divalent third-row transition metal oxide for several reasons. In the usual process the anion required for the desired material (e.g. sulfide) is generated slowly in the form of a strongly chelated metal so that the constituent cations and anions are assembled into a thin film by an ion-by-ion deposition process. Since oxide ions are protonated by water, the direct solution growth metal oxide films from aqueous is precluded for most metals. However, hydroxides can be prepared by solution growth by using the hydrolysis of urea to slowly raise solution pH. Unfortunately, for the metals of interest in this study, nickel and zinc, this metal would lead to deposition of carbonate rather than the hydroxides. Therefore, in this investigation, a new method was developed for solution growth of nickel hydroxide. This new process takes advantage of the strong complexation of nickel by ammonia ($K_f [\text{Ni}(\text{NH}_3)_6]^{2+} = 5.5 \times 10^8$ ⁶⁵) to overcome the insolubility of Ni(OH)₂ in water ($K_{sp} = 2.0 \times 10^{-15}$ ⁶⁶). Once a solution is saturated with Ni(OH)₂ it is susceptible to deposition of this metal hydroxide as the ammonia evaporates from the solution (see Equation 7).

Addition of nickel hydroxide to concentrated ammonia leads to formation of a dark blue color attributable to $[\text{Ni}(\text{NH}_3)_6]^{2+}$.

2. Determination of Solubility of $\text{Ni}(\text{OH})_2$ in Concentrated Aqueous Ammonia:

The concentration of nickel hexammine was determined by measuring the weight of $\text{Ni}(\text{OH})_2$ deposited after complete evaporation of the solvent, and drying of the solid under vacuum. The experiment was performed five times in the same conditions. The concentrations calculated are listed in table 7.

Table 7. $[\text{Ni}(\text{NH}_3)_6]^{2+}$ concentrations (mol/L):

Weight of $\text{Ni}(\text{OH})_2$ dissolved in 40 mL ammonia solution (grams)	0.517	0.545	0.501	0.529	0.488
$[[\text{Ni}(\text{NH}_3)_6]^{2+}]$ (mol/L)	0.139	0.147	0.135	0.143	0.132

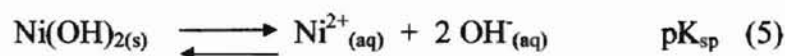
The standard deviation s is determined to characterize the variability of the experimental Ni^{2+} concentrations listed in table 7. The average $[\text{Ni}^{2+}]_{\text{av}}$ calculated is 0.139 mol/L and s computed with the 5 experimental $[\text{Ni}^{2+}]$ concentrations is $s = 6.02 \times 10^{-3}$, s being as follows:

$$S = \sqrt{\frac{\sum_i^N ([\text{Ni}^{2+}]_i - [\text{Ni}^{2+}]_{\text{av}})^2}{N - 1}}$$

i = integer between 1 and N number of experimental figures

N = number of experimental figures = 5

The chemical equation representing the overall equilibrium (see Equation 7) is the sum of the Ni(OH)₂ dissolution reaction (see Equation 5) and the Ni(II) complexation reaction with ammonia (see Equation 6).



$$P_s = -\log \left(\frac{[\text{Ni(NH}_3)_6]^{2+} [\text{OH}^{-}]_{tot}^2}{[\text{NH}_3]^6} \right) \quad (8)$$

Where [Ni(NH₃)₆²⁺], [NH₃] and [OH⁻] are concentrations in mol/L

P_s is computed by using the average [Ni(NH₃)₆²⁺] concentration determined above (0.139 M). [OH⁻]_{tot} in the ammonia solution after saturation with Ni(OH)₂, is determined by measuring the pH (13.7). [NH₃] is the concentration after complexation of Ni²⁺ with 6 ammonia equivalents, where [NH₃]_{initial} is the concentration of the initial ammonium hydroxide solution⁴⁶. [NH₃]_{equilibrium} was calculated by subtracting the concentration of [NH₄⁺] formed at equilibrium from the remaining as follows:

$$[\text{NH}_3]_{\text{equilibrium}} = [\text{NH}_3] - [\text{NH}_4^+]_{\text{equilibrium}}$$

$$[\text{NH}_3]_{\text{equilibrium}} = ([\text{NH}_3]_{\text{initial}} - 6[\text{Ni}^{2+}]) - ([\text{OH}^{-}]_{\text{tot}} - 2[\text{Ni}^{2+}])$$

$$= 14.53 - 6 \times 0.139 - 10^{-0.3} + 2 \times 0.139$$

$$= 13.47 \text{ M}$$

By using Equation 8, P_s can be easily calculated and is found to be 8.23

The pK_s determined experimentally is significantly higher than the theoretical value of 6.0 calculated as the sum of the pK_f and pK_{sp}. In other words, the solubility of nickel hydroxide in conc. ammonia is about two orders lower than predicted. The theoretical

value does assume ideal behavior (i.e. low concentrations where activity is proportional to concentration) and zero ionic strength. Since the experimental conditions deviate significantly from these assumptions, this could account for a discrepancy in the values of pKs. As well, assumptions made concerning the speciation of Ni(OH)_2 in the aqueous ammonia solution could be enormous- for example, formation of $[\text{Ni(OH)(NH}_3)_5]^+$ complex could lead to significant perturbation of the experimental result. Also the concentration of water in concentrated ammonia is reduced to 40 M from 56 M for pure water this too, could have a major effect on solubility. Evaporation of ammonia during the dissolution of Ni(OH)_2 may also play a minor role in the depressing the final nickel concentration. The results do also show, however, that simple use of formation constant and solubility products do not make an adequate prediction of the solubility of the metal hydroxides in concentrated ammonia.

The solution growth of Ni(OH)_2 depends on the slow formation of hexa-aqua nickel (II) conc. as the ammonia evaporates from solution. Either this ion, or an intermediate ammonia complex $[\text{Ni(H}_2\text{O)}_x(\text{NH}_3)_{(6-x)}]^{2+}$, interacts with hydroxide ion to form a hydroxide complex, probably occurs by deprotonation of the coordinated aqua ligand. The addition of a second hydroxide ion or deprotonation of a second aqua ligand could generate a Ni(OH)_2 complex that would be prone to precipitation. For solution growth of nickel hydroxide films to occur, it is desirable that the second reaction occur on the surface of the substrate or that the putative Ni(OH)_2 complex diffuse and deposit precipitating from the bulk solution.

3. Ni(OH)₂ Thin Film From Solution Growth Method:

The rate of deposition of Ni(OH)₂ was determined by placing 30 ml of Ni(OH)₂-saturated ammonia in eight identical beakers. The amount of nickel hydroxide deposited after various time intervals was determined by emptying the remaining solution from the beaker, placing under vacuum overnight, and weighing. After 120 hours, the solution was colorless indicating that all the nickel(II) initially dissolved had precipitated. The plot of Ni(OH)₂ film weight versus time is shown in Figure 19. The deposition occurs progressively at a almost constant rate up to 90 hours, then slows down and stops after 120mn. The deposition does occur as a solution growth process and yields homogeneous pale green films on the sides of the beaker.

The morphology of Nickel hydroxide prepared from the ammonia solution is quite unusual, as illustrated on the scanning electron micrograph shown in Figure 20. Large spheres with a diameter of 3.8 μm appear to consist of extremely small needles of Ni(OH)₂. Despite the very porous looking microstructure and a rather small particle size the surface area measurement listed in Table 8 is surprisingly small possibly due to the adsorbed and intercalated water molecules.

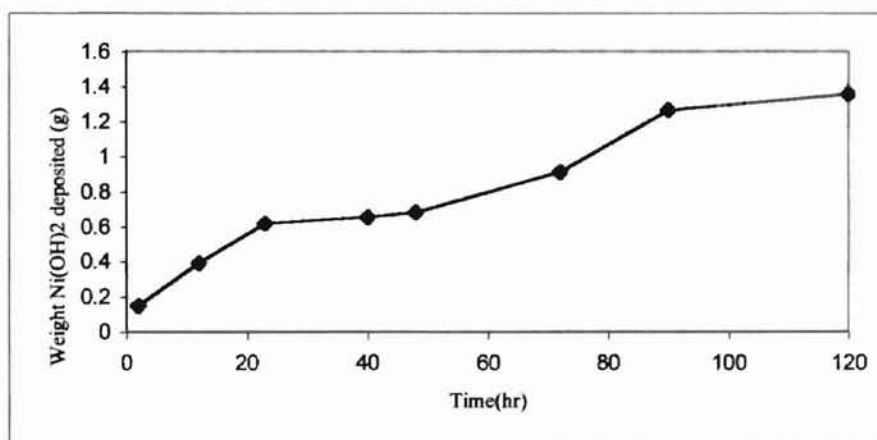


Figure 19. Nickel Hydroxide Deposition Rate

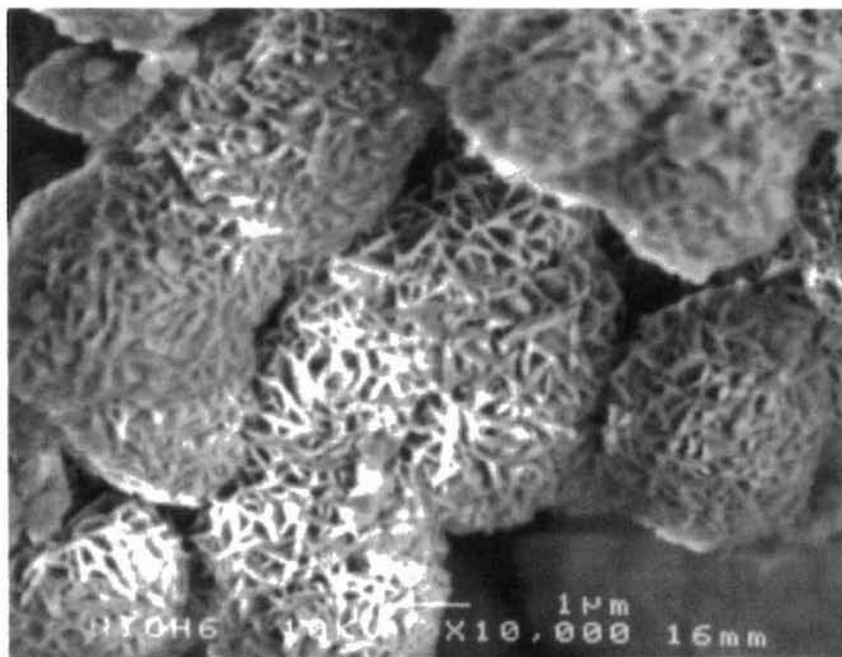


Figure 20. SEM of β -Ni(OH)₂ from Solution Growth

A typical X-ray diffraction pattern for nickel hydroxide synthesized by the ammonia solution growth is shown in Fig. 21 (a) with a common Ni(OH)₂ pattern obtained from another precipitation method ⁶³ Fig. 21 (b) as a basis for comparison. The considerably higher intensity of certain reflections of the ammonia grown hydroxide is an indication of a larger crystallite size in specific crystallographic directions including [001], [101], and [102]. The increase in crystallite size is also accompanied by a decrease of the NiO interplanar distance from 4.59 Å to 4.72 Å, as evidenced by a shift towards smaller d of the 001 plane reflection peak. As a result of the d_{001} change, the d-spacings of the peaks including (101) and (102) are also slightly displaced but to a lesser extent. This suggests the slow precipitation of Ni(OH)₂ from aqueous ammonia yields a highly ordered layered compound, in contrast with the poorly crystallized Ni(OH)₂ from the rapid precipitation of a nickel nitrate solution. Previous work on the preparation of nickel hydroxide from hydrothermal treatment reported ⁶⁷ an identical X-ray Ni(OH)₂ pattern and

microstructural characteristics. This two-step method consisted of hydrothermally treating at 200°C an aqueous suspension of turbostratic α -Ni(OH)₂ previously prepared by the precipitation by treatment of a nickel nitrate solution with base⁶⁷.

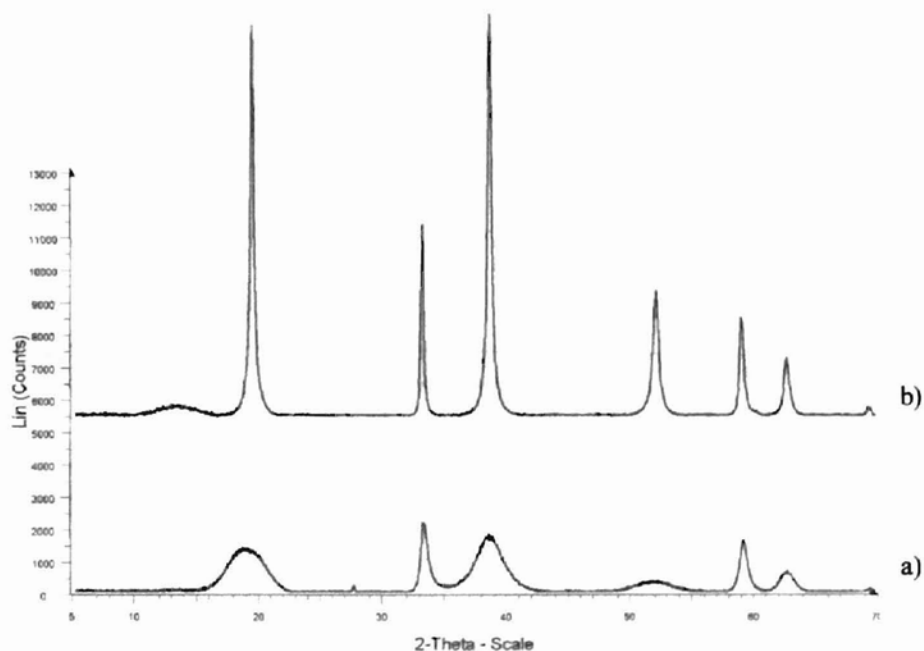


Figure 21. XRD of β -Ni(OH)₂ from Solution Growth Method (b), and from Precipitation Method from a Ni(NO₃)₂ solution with Strong Base(a)

Infrared spectroscopy is a good indicator of short-range structure and very useful for characterizing Ni(OH)₂ phases. The formation of the β form of Ni(OH)₂ demonstrated by using X-ray diffraction was confirmed in the infrared spectrum showed in Figure 22. The existence of an intense sharp absorption at 3642cm⁻¹ is characteristic of O-H stretching vibration, ν_{OH} , of non hydrogen-bonded OH groups. The broad shoulder at 3400cm⁻¹ is attributed to the ν_{OH} of hydrogen-bonded OH groups of adsorbed water molecules. A weak irregular band from 1500 to 1696 cm⁻¹ includes the water angular deformation at 1653 cm⁻¹ and adsorbed ammonia molecules deformation vibration.

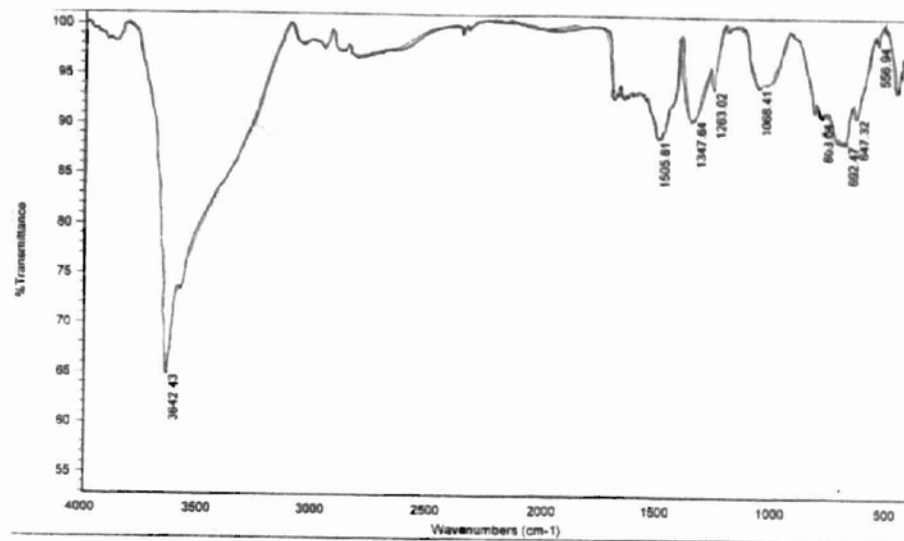


Figure 22. Infrared Spectrum of β -Ni(OH)₂ from Solution Growth Method

The thermal decomposition pattern shown in Figure 23 is very similar to those published in early studies^{58, 68, 69}. Gradual elimination of adsorbed molecules such as water constitutes the first weight loss. The slightly endothermic process stops at 180°C. The dehydrated sample then undergoes dehydration to yield NiO at 500°C with release of heat. The decomposition of Ni(OH)₂ grown from the sulfate or nitrate salt solutions⁵³ usually extends over a wider temperature range necessary to pyrolyze the adsorbed anions such as SO₄²⁻, CO₃²⁻ and NO₃⁻ present in the mother solution.

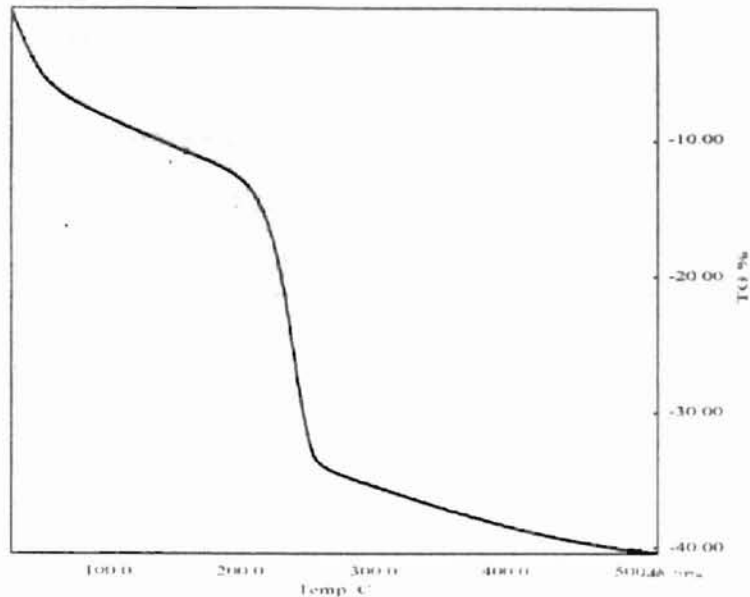


Figure 23. TGA of β -Ni(OH)₂ from Solution Growth Method

4. Aluminum Doped Alpha Ni(OH)₂:

The success of the solution growth process for β -Ni(OH)₂ prompted an investigation of the possibility of forming α -Ni(OH)₂ by solution growth. Since it was known that substitution of aluminum for nickel ions can influence the formation of α -Ni(OH)₂, aluminum ions were introduced into the solution growth bath. The first approach to accomplish this that was investigated was the saturation of the solution growth solution of concentrated aqueous ammonia with both nickel and aluminum hydroxides. The solubility of the latter species is much lower than Ni(OH)₂ and was determined accurately by saturated pure concentrated Ni(OH)₂ with Al(OH)₃. Three estimates of [Al(OH)₄]⁻ concentration were obtained by using the same approach as that employed for [Ni(NH₃)₆]²⁺. The results are listed in Table 9. The average [Al(OH)₄]⁻ concentration calculated is 2×10^{-2} M with a standard deviation of $s = 9.22 \times 10^{-4}$.

Table 8. Surface Area of β and α -Ni(OH)₂ from Solution Growth Method

Compound	Surface area (m ² /g)
β -Ni(OH) ₂ from solution growth	20.6
α Ni _{0.87} Al _{0.13} (OH) _{2.13}	37.1
α Ni(OH) ₂ -NaAl(OH) ₄	28.3

Evaporation of ammonia from the Ni(OH)₂/Al(OH)₃ solution in concentrated ammonia led to co-precipitation of the metal hydroxides as a single phase, Ni_(1-x)Al_x(OH)_(2+x). Assuming that all the nickel and aluminum ions are incorporated into the precipitate, x can be calculated from the relative solubilities of the metals. This gives a formula of Ni_{0.87}Al_{0.13}(OH)_{2.13} for the precipitate. The X-ray pattern of this material (Figure 24 (a)) demonstrates that the aluminum content is sufficiently high for formation of the α -Ni(OH)₂ structure.

Table 9. Concentration of [Al(OH)₄]⁻ in Concentrated Aqueous Ammonia (mol/L):

[[Al(OH) ₄] ⁻]	0.0201	0.0193	0.0205
--	--------	--------	--------

The XRD reflections are broad and asymmetrical indicating the disordered nature of the stacking sequences of the material ⁷⁰. The particle size calculated from the scanning

electron micrograph ranges from 0.20 to 1.7 μm , the largest particles visibly consist of aggregates of smaller spherical particles (not shown). Alpha $\text{Ni}(\text{OH})_2$ can be indexed on a hexagonal cell⁶³ whose lattice parameters can be computed using the following formula:

$$\frac{1}{d_{hkl}^2} = \frac{1}{a^2} (h^2 + hk + l^2) + \frac{l^2}{c^2}$$

h , k , l are the Miller indices which define a crystallographic plane in three dimensions. The reflections at $2\theta=11.6$ ($d_{003}=7.63\text{\AA}$) and 35.1 ($d_{102}=2.55\text{\AA}$) were used to determine the cell parameters c and a : $a=3.5\text{\AA}$, $c=22.9\text{\AA}$. The infrared spectrum of $\text{Ni}_{0.87}\text{Al}_{0.13}(\text{OH})_{2.13}$ shown in Figure 25 shows the characteristic broad ν_{OH} absorption band at 3483 cm^{-1} for the hydrogen-bonded hydroxyl group of $\alpha\text{-Ni}(\text{OH})_2$.

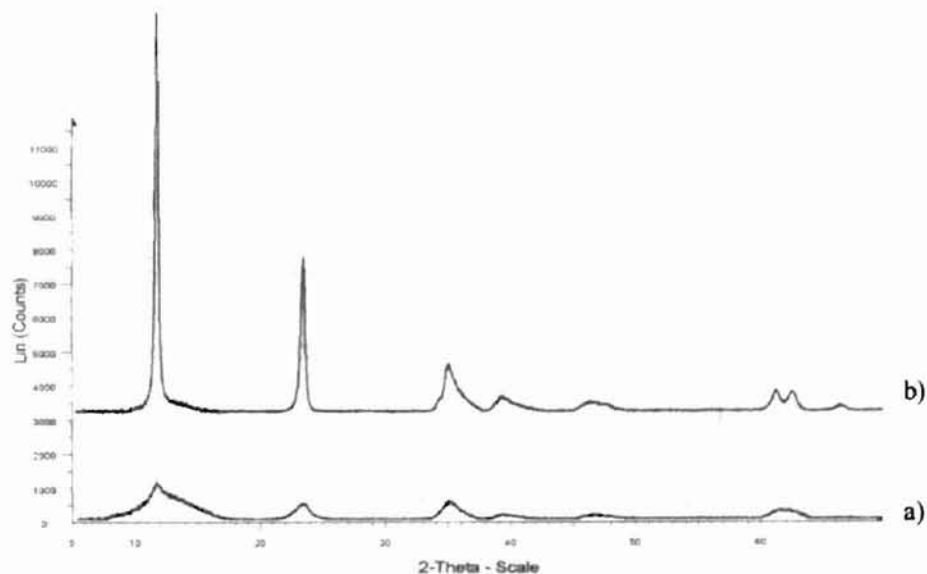


Figure 24. XRD of $\text{Ni}_{(1-x)}\text{Al}_x(\text{OH})_{(2+x)}$ (a), and $\text{Ni}(\text{OH})_2\text{-NaAl}(\text{OH})_4$ (b)

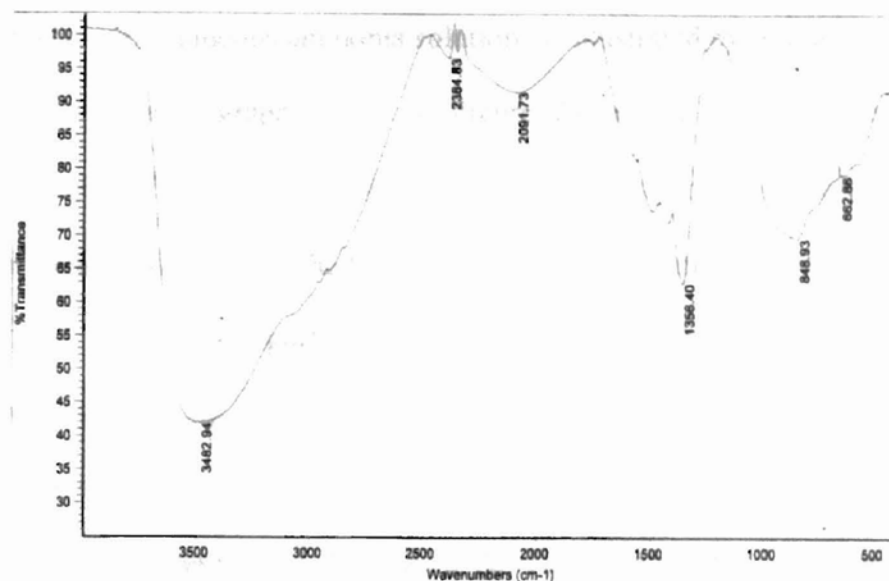


Figure 25. Infrared Spectrum of $\text{Ni}_{(1-x)}\text{Al}_x(\text{OH})_{(2+x)}$

Doping of $\text{Ni}(\text{OH})_2$ with aluminum was also achieved by simply introducing sodium aluminate into the solution growth bath. The advantage of this approach resides in the fact that it provides better control of aluminum concentration than saturation of ammonia solution with aluminum hydroxide. Thus it is possible to readily determine the $\text{Ni}(\text{II})/\text{Al}(\text{III})$ ratio required for formation of $\alpha\text{-Ni}(\text{OH})_2$. However, it was necessary to collect the green precipitate before complete evaporation of the solvent to prevent crystallization of excess sodium aluminate onto the nickel hydroxide precipitate.

The various X-ray patterns of $\text{Ni}(\text{OH})_2$ from the growth solution containing $\text{NaAl}(\text{OH})_4$ (0.33M) are shown in Figure 26. The addition of 1 ml of $\text{NaAl}(\text{OH})_4$ (0.33M) (see Fig. 26. (b)) was sufficient to precipitate some $\alpha\text{-Ni}(\text{OH})_2$ along with the predominantly-formed β phase. The formation of $\alpha\text{-Ni}(\text{OH})_2$ is progressively favored as the volume of $\text{NaAl}(\text{OH})_4$ introduced increases (see Fig. 26 (c) and (d)). A pure

crystalline alpha form is precipitated from a solution containing 6 ml of NaAl(OH)_4 and 40 mL of Ni(OH)_2 -conc. aqueous ammonia solution, as illustrated by Figure 26. (e). The transmission electron micrograph shown in Figure 27 reveals the presence of large ($0.45\mu\text{m}$) spherical Ni(OH)_2 particles along with blocks of materials composed of sheets that are delaminated at the edges. The $[\text{Ni}^{2+}]:[\text{Al}^{3+}]$ ratio for formation of the pure alpha-phase was 2.81:1, which is significantly lower than the 6.69:1 ratio determined for $\text{Ni}_{0.87}\text{Al}_{0.17}(\text{OH})_{2.13}$. By using $[\text{Ni}(\text{NH}_3)_6]^{2+}$ and $[\text{Al(OH)}_4]^-$. The lattice parameters of the precipitated layered double hydroxide c and a were determined using the 003 and 110 reflections ($a=2d_{110}$) values: $a=3.5 \text{ \AA}$; $c=23.2 \text{ \AA}$. The a parameter is higher than the typical 3.0 to 3.1 \AA reported in the literature^{63, 70}. Since Al(III) is smaller than Ni(II), this indicates the content of Al(III) necessary to stabilize the alpha structure by the solution growth method is smaller than that required by the nitrate solution precipitation method. In the latter method, the LDH is obtained at a ratio of Ni:Al of 6.69:1. In the 2.6-3.2 \AA region, a broad asymmetrical band, typical of turbostratic structures is seen. These X-ray reflections indicate the disordered nature of the NiO_2 slabs stacking.

The presence of aluminum ions not only causes the formation of $\alpha\text{-Ni(OH)}_2$ but it also has a profound effect on the morphology of the product. Unfortunately, the aluminum-containing chemical baths are not amenable to solution growth of $\alpha\text{-Ni(OH)}_2$ thin films. However this failure is compensated by the ability to form free-standing films at the solution/air interface, along with additional precipitated material at the bottom of the bath. Presumably, the difference from the aluminum-free deposition is a result of substitution of aluminum ions for nickel ions in the Ni(OH)_2 as it forms.

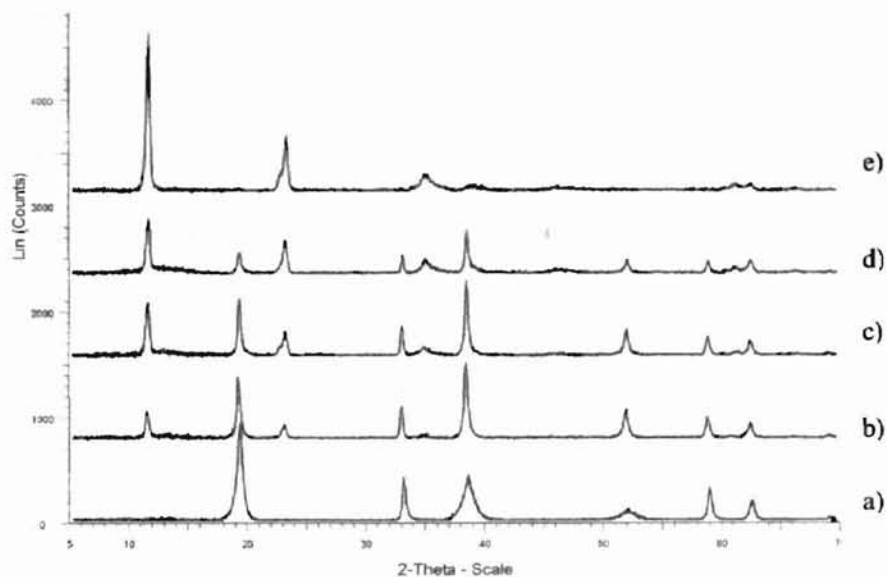


Figure 26. XRD of Solid from 40 mL Ni(OH)₂-NH₄OH (a), with 1 mL (b), 2 mL (c), 4 mL (d), and 6 mL (e) of NaAl(OH)₄ (0.33 M) Solution

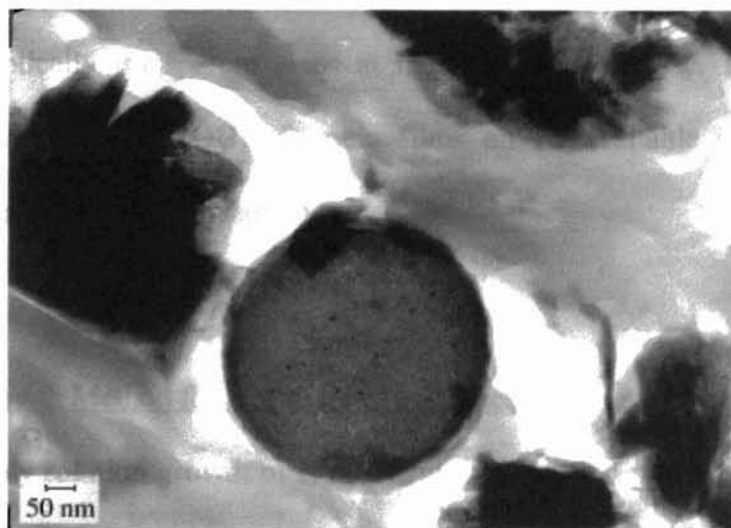


Figure 27. TEM of Ni(OH)₂-NaAl(OH)₄ Precipitate

This would produce positively charged particles that would repel each other and resist aggregation into a precipitate on a film. However, as the ammonia rapidly evaporates from solution the particles are carried to the air/solution interface where they aggregate

into a film of average thickness 0.10 mm. Possibly, the linking of the particles occurs as the ammonia is lost from nickel ions on the surface of the particles causing particles to link together by formation of hydroxide bridges. Once the original film forms as a skin over the surface of the solution, it continues to grow thicker as more material deposits on its bottom. The net result is an opaque green film that is smooth on the upper surface and rough on the lower side due to random aggregation of particles. The films are somewhat brittle but can be removed from the deposition bath and manipulated carefully by hand. Thus, free-standing films of aluminum-stabilized Ni(OH)_2 were readily prepared and these could be promising electrode materials.

While in the absence of aluminum, the Ni(OH)_2 /concentrated ammonia solution mainly deposits thin coatings on the container wall or suspended substrates, it also forms extremely thin, optically transparent skins at the air-water interface. Presumably the thinness is a result of the Ni(OH)_2 forming films on all available surfaces with a preference for the solid-liquid interface.

5. Solution Growth Method for Nickel Ferrite Synthesis:

In order to apply solution growth of Ni(OH)_2 to the modified powder process, it was necessary to use a container whose walls were resistant to the growth of the nickel hydroxide film. It was found that a plastic such as polypropylene was suitable and allowed the deposition to occur only on the non-oxide substrate. Thus, a non-crystalline iron oxide and sufficient Ni(OH)_2 concentrated ammonia solution to provide the necessary amount of nickel for stoichiometric NiFe_2O_4 were placed in an open polypropylene bottle. The mixture was rotated slowly on a roller mill to ensure even coating of the iron oxide

particles. In this manner a ferrite precursor was obtained that converted to nano-sized, high surface area NiFe_2O_4 at 900°C (see Table 10). The average crystallite size obtained from diffraction line broadening of X-ray pattern peaks is 22.4 nm, and the average particle size estimated from SEM micrographs is 150 nm. The as-prepared precursor morphology is illustrated by the scanning electron micrograph shown in Figure 28. Large $\beta\text{-Ni(OH)}_2$ aggregates are not observable indicating homogeneous coating of Ni(OH)_2 onto the $\alpha\text{-Fe}_2\text{O}_3$ particles. Upon pyrolysis to 900°C little change in particle size is observed (see Figure 29). This indicates the sintering process, which would have caused the particle size to increase, was greatly minimized by the homogeneous NiO coating of the iron oxide particles.

Table 10. Surface Area Measurements of $\text{Ni(OH)}_2\text{-}\alpha\text{-Fe}_2\text{O}_3$ Precursor and NiFe_2O_4 :

Processing temperature	Surface area (m^2/g)
25	103.5
900	47.1

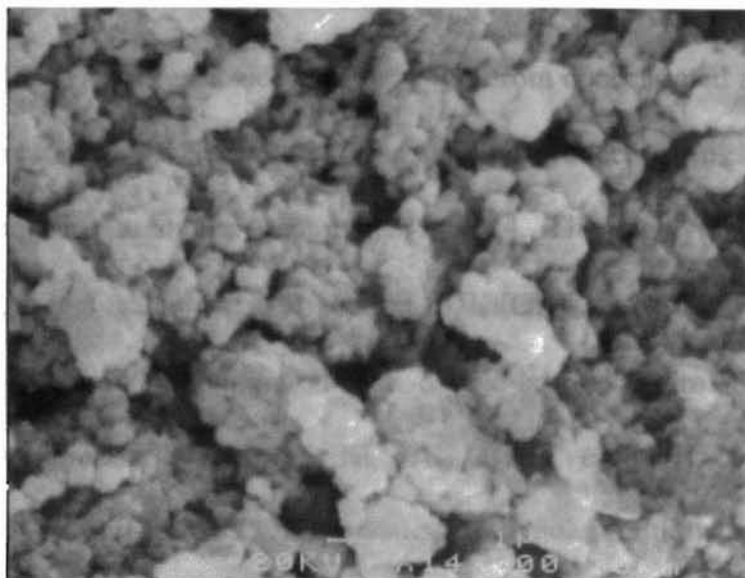


Figure 28. SEM of as-prepared Ni(OH)₂- γ -Fe₂O₃

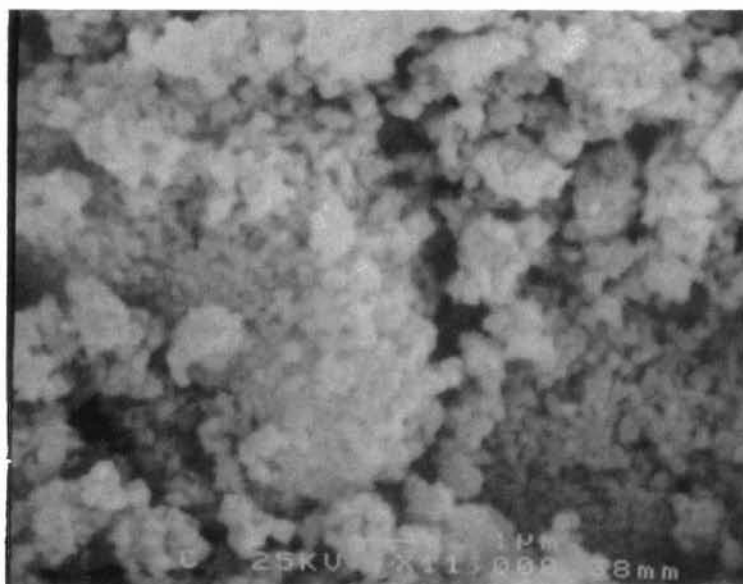


Figure 29. SEM of NiFe₂O₄ from Pyrolysis of Ni(OH)₂- γ -Fe₂O₃ Precursor at 900°C

6. Conclusion:

Pure β -Ni(OH)₂ films were successfully grown from concentrated aqueous ammonia previously saturated with Ni(OH)₂. The solubility product of nickel hydroxide in concentrated aqueous ammonia determined is 8.24. The highly crystalline material consists of large aggregates of small needles of Ni(OH)₂. α -Ni(OH)₂ was successfully stabilized by doping with aluminum. The double-layered hydroxide prepared from saturation with aluminum hydroxide is Ni_{0.87}Al_{0.13}(OH)_{2.13}. Ni(OH)₂ being an electrode material of great interest to battery manufacturers, the solution growth process seems to be a promising technique to deposit Ni(OH)₂ films directly onto a substrate for application as electrode material.

The solution growth method for Ni(OH)₂ synthesis was successfully applied to the preparation of a nickel ferrite precursor, which produced fine NiFe₂O₄ with particle size only a few nm larger than the precursor particle size at 450°C. The fact that the sintering process was greatly reduced indicates the quality of the NiO coating onto iron oxide particles was remarkable.

REFERENCES

1. D. Segal "Chemical Synthesis of Advanced Ceramic Materials" Cambridge University Press, **1991**.
2. C.D. Chandler, C. Roger, M.J. Hampden-Smith, Chem. Rev., **1993**, Vol. 93, pp 1205.
3. P.A. Lane, P.J. Wright, M.J. Crosbie, A.C. Jones, T.J. Leedham, *J. Cryst. Growth.*, **1998**, Vol. 192 (3/4), pp 423-429.
4. A.C. Jones, Chem. Vap. Deposition. **1998**, Vol. 4, No. 5, pp 169-179.
5. P. Barboux, J. M. Tarascon, L.H. Greene, G.W. Hull, B.G. Bagley, *J. Appl. Phys.*, **1988**, Vol. 63, No 8 (Pt. 1), pp 2725-2729.
6. K. Oda, T. Yoshio, K. Hirata, K. O-oka, K. Takahashi, *J. Jpn. Soc. Powder Metall.*, **1982**, Vol. 29, No. 5, pp 170.
7. Y. Suwa, S. Hirano, K. Itozawa, S. Naka in "*Ferrites – Proceedings of the International Conference*", Tokyo, Japan, **1980**, pp 23-26.
8. S. Hirano, J. Watanabe, S. Naka, "Synthesis and properties of CoFe_2O_4 by Hydrolysis of Metal-Acetylacetonates" in *Advances in Ceramics*, F.F.Y. Wang ed., Am. Ceram. Soc., Columbus, OH, **1985**, Vol. 15, pp 65-71.
9. K. Higuchi, S. Naka, S. Hirano, *Adv. Ceram. Mater.*, **1986**, Vol. 1, No. 1, pp 104
10. W.J. Schuele, V.D. Deetschreek, "Fine Ferrite Particles in Ultrafine Particles", W. E. Kuhn, H. Lamprey and C. Sheer eds., John Willey & Sons, Inc., New York, , **1963**, pp 218-235.

11. B.K. Das, "Development and Preparation of Solid Ferrites" in Preparation and Characterization of Materials, J.M. Honig and C.N.R. Rao ed., Academic Press, New York, **1981**, pp 75-100.
12. S.I. Hirano, J.I. Watanabe, and S. Naka, *Advances in Ceramics "Fourth International Conference on Ferrites"* Part 1. **1984**, pp 65-63.
13. D.G. Wickham, E.R. Whipple, and E.G. Larson, *J. Inorg. Nucl. Chem.*, **1960**, Vol. 14, pp 217.
14. A.W. Apblett, L.A. Cubano, G.D. Georgieva, and J.T. Mague, *Chem. Mater.*, **1996**, Vol. 8, No 3, pp 650-655.
15. A.W. Apblett, M.L. Breen, and E.H. Walker, "Synthesis of Nickel Ferrite Using Liquid Metal Carboxylates", *Mater. Chem.*, **1998**, Vol. 10, No 1, pp 265-269.
16. E.H. Walker, A.W. Apblett, "Innovative Processing and Synthesis of Ceramics, Glasses, and Composites II" *Ceram. Trans.*, **1999**, Vol. 94, pp 205-213.
17. D.W. Hopkins, *J. Electrochem. Soc.*, **1949**, Vol. 96, pp 195.
18. A.W. Apblett, L.E. Reinhardt, E.H. Walker, *Comments Inorg. Chem.*, **1998**, Vol. 20, No 2-3, pp 83-99.
19. D. Lincot, R. Ortega-Borges, and M. Froment, *Appl. Phys. Lett.*, 1994, Vol. 54, No. 5, pp 569-571.
20. I. Yu, T. Isobe and M. Senna, *Mater. Res. Bull.*, **1995**, Vol. 30, No. 8, pp. 975-980.
21. N. C. Sharma, D. K. Pandya, H. K. Sehgal, and K. L. Chopra, *Thin Solid Films*, **1977**, Vol. 42, pp. 383-391.

22. T. Tadokoro, S. Ohta, T. Ishiguro, Y. Ichinose, S. Kobayashi, and N. Yamamoto, *J. Cryst. Growth*, **1993**, Vol. 130, pp 29.
23. S. Gits, M.C. Robert and F. Lefauchaux, *J. Cryst. Growth*, **1985**, Vol. 71, pp 203-208.
24. P. Oliva, J. Leonardi, J.F. Laurent, C. Delmas, J.J. Braconnier, M. Figlarz, F. Fievet, A. Guibert, *J. Power Sources*, **1982**, Vol. 8, pp 229-255.
25. Handbook of Preparative Inorganic Chemistry, G. Bauer, Academic Press, Vol. 2, pp 1500-1501.
26. Osaki M., Kratochvil S., and Matijevic E., *J. Colloid Interface Sci.*, **1984**, Vol. 102, No. 1, pp 146-151.
27. F.X.N.M. Kools, D. Stoppels in Ferrites, Kirk-Othmar's Encyclopedia of Chemical Technology, J. Kroschwitz and M. Howe-Grant ed., John Wiley & Sons, Inc., New York, **1993**, Vol. 10, pp 381-413.
28. J.J. Went, E.W. Gorter, *Philips Techn. Rev.*, **1951-1952**, Vol. 13, pp 181.
29. K. Sreekumar, T.M. Jyothi, M.B. Talawar, B.P. Kiran, B.S. Rao, S. Sugunan, *J. Molec. Catal. A*, **2000**, Vol. 152, pp 225-236.
30. K. Sreekumar, T. Raja, B.P. Kiran, S. Sugunan, B.S. Rao, *Appl. Catal. A*, **1999**, Vol. 182, pp 327-336.
31. W.S. Chen and M.D. Lee, *Appl. Catal. A*, **1992**, Vol. 83, pp 201-211.
32. W.L. Kehl and R.J. Rennard Jr, *Goodrich-Gulf Chemicals, Inc.*, US patent 3,450,787, **1969**, 6 pp.
33. W.L. Kehl and R.J. Rennard Jr, *Goodrich-Gulf Chemicals, Inc.*, US patent 3,450,788, **1969**, 6 pp.

34. C.S. Narasimhan and C.S. Swamy, *Applied Catalysis*, **1982**, Vol. 2, pp 315-328.
35. G.C Kuczynski, *Ferrites: Proceedings of the International Conference*, **1971**, pp 87-95.
36. E. Karmazsin, P. Satre and P. Vergnon, *J. Thermal Anal.*, **1983**, Vol. 28, pp 279-284.
37. G. Hagg, *Z. Phys. Chem.*, **1935**, Vol. 29, pp 95.
38. S. Kachi, N. Nakanishi, K. Kosuge, H. Hiramatsu, and M. Kiyama, *Ferrites: Proceedings of the International Conference*, **1971**, pp 141-143.
39. V.V. Boldyrev, M. Bulens, and B. Delmon, *The Control of the Reactivity of Solids*, Elsevier scientific Publishing Company, **1979**, pp 32-38.
40. K.S. Rane, V.M.S. Verenkar, and P.Y. Sawant, *J. Mat. Science, Mat. Elect.*, **1999**, Vol. 10, pp 133-140.
41. H.J. Hunh, *Z. Chem.*, **1987**, Vol. 27, pp 334-335.
42. J.J. Shrotri, a.g. Bagul, s.d. Kulkarni, C.E. Deshpande, and S.K. Date, in "*Proc. VI Int. Conf. On Ferrites*" Tokyo Japan, **1992**, pp 404.
43. G. A.M. Hussien, *Thermochimica Acta*, **1991**, Vol. 186, pp 187-197.
44. H.M. Ismail, *J. Anal. Appl. Pyrolysis*, **1991**, Vol. 21, pp 315-326.
45. A.R. Baron et al. , *Chem. of Mater.*, **1996**, Vol. 8, No 9, pp 2331-2340.
46. Lange`s Handbook of Chemistry, 14th edition. Mc Graw-Hill, Inc., **1992**
47. B.E. Warren, *Progress in Metal Physics*, **1959**, Vol. 8, pp 147.
48. *WIN-CRYSIZE, Crystallite Size and Microstrain, User`s Manual*, Bruker Analytical X-ray Systems, pp 25-29.

49. A.K. Galwey, "The Reactivity of Solids in Thermal Decomposition Reactions", *Reactivity of Solids: Past, Present, and future*. Edited by V.V. Boldyrev, **1997**, pp 17.
50. J.I. Langford, A. Boultif, J.P. Auffredic, D. Louër, *J. Appl. Cryst.*, **1993**, Vol. 26, pp 22-23.
51. N. Audebrand, J.P. Auffredic, and D. Louër, *Chem. Mater.*, **1998**, Vol. 10, pp 2450-2461.
52. H. Bode, K. Dehmelt, and J. Witte, *Electrochem. Acta*, **1966**, Vol. 11, No 8, pp 1079-1087.
53. C. Delmas, C. Faure, L. Gautier, L. Guerlou-Demourgues and A. Rougier, *Phil. Trans. R. Soc. Lond. A*, **1996**, Vol. 354, pp 1545-1554.
54. R.M. Dell, NATO ASI Ser., Ser. E, 101 (Solid State Batteries), **1985**, pp 319-336.
55. S.O. Aulin, *Svenska Ackumulator Aktiebolaget Jungner*, US patent 3,305,401, **1963**, 3 pp.
56. B. Aladjov, The Hall Chemical Company, **1998**, 5 pp.
57. P.V. Kamath, N.Y. Vasanthacharya, *J. Appl. Electrochem.*, **1992**, Vol. 22, pp 483-485.
58. M.B.J.G. Freitas, *J. Power Sources*, **2001**, Vol. 93, pp 163-173.
59. O. Glemser, in "Handbook of Preparative Inorganic Chemistry", Vol. II (Edited by G. Brauer), Academic Press, **1965**, pp 1549.
60. Y. Zhang, Z. Zhou, and J. Yan, *J. Power Sources*, **1998**, Vol. 75, pp 283-287
61. A. Merlin, *C. R. Acad. Sci., Paris*, **1953**, Vol. 236, pp 1892.

62. D.Y. Shin *et al.*, Samsung Display Devices Co., Ltd., US patent 5,840,269, **1998**, 5 pp.
63. P.V. Kamath, and others, *J. Electrochem. Soc.*, **1994**, Vol. 141, No. 11, pp 2956-2959.
64. C. Delmas, J.J. Braconnier, Y. Borthomieu, and M. Figlarz, *Solid State Ionics*, **1988**, Vol. 28-30, pp 1132-1137.
65. J.A Dean, "Solubility Products" in Lange's Handbook of Chemistry 14th Ed. Mc Graw- Hill. New York, **1992**, pp 8.7
66. J.A. Dean, "Cumulative Formation Constants for Metal Complexed with Inorganic Ligands", in Lange's Handbook of Chemistry 14th Ed. Mc Graw- Hill. New York, **1992**, pp 8.84
67. F. Fievet and M. Figlarz, *J. Catal.*, **1975**, Vol. 39, pp 350-357.
68. C. Cabannes-Ott, *Ann. Chim.*, **1960**, Vol. 5, pp 917-920.
69. B. Mani, J.P. Neufville, *J. Electrochem. Soc.*, **1988**, Vol. 135, pp 800.
70. G.A. Caravaggio, C. Detellier, and Z. Wronski, *J. Mater. Chem.*, **2001**, Vol. 11, No. 3, pp 912-921.

VITA

Audrey Celine Vecoven

Candidate for the Degree of

Master of Science

Thesis: INNOVATIVE PROCESSES FOR METAL OXIDE CERAMIC
SYNTHESIS

Major Field: Chemistry

Biographical:

Education: Received Bachelor of Science Degree in Chemistry from the University of Lille I, France, June, 1998; completed the requirements for the Master of Science degree at Oklahoma State University, Stillwater, Oklahoma in December, 2001.

Experience: Analytical technician at the Ciment d'Obourg, Belgium, June 1996 and 1997. Intern at The SOCOR, August to December 1997, conducted waste water and fuel sample preparation and analysis. Employed by Oklahoma State University, Chemistry Department as a Graduate teaching, research assistant.

Professional Memberships: American Chemical Society